IMPROVED SYNTHETIC METHODS FOR PATCHY PARTICLES

A Thesis

by

NINA OLEGOVNA IVANOVA

Submitted to the Office of Graduate Studies of
Texas A&M University
in partial fulfillment of the requirements for the degree of

MASTER OF SCIENCE

December 2011

Major Subject: Mechanical Engineering

IMPROVED SYNTHETIC METHODS FOR PATCHY PARTICLES

A Thesis

by

NINA OLEGOVNA IVANOVA

Submitted to the Office of Graduate Studies of
Texas A&M University
in partial fulfillment of the requirements for the degree of

MASTER OF SCIENCE

Approved by:

Chair of Committee,	Nicole Zacharia
Committee Members,	Molly Gentleman
	Zhengdong Cheng
Head of Department,	Jerald A. Caton

December 2011

Major Subject: Mechanical Engineering

ABSTRACT

Improved Synthetic Methods for Patchy Particles. (December 2011)

Nina Olegovna Ivanova, Hon.B.S., University of Toronto

Chair of Advisory Committee: Dr. Nicole Zacharia

Patchy particles are patterned particles with at least one well-defined patch that can have highly directional and strongly anisotropic interactions with other particles or surfaces. Multiple theoretical studies point to interesting self-assembly of these particles into superstructures and, as a result, a multitude of possible applications. However, reliable synthetic methods for patchy particles, especially at the sub-micron level, are still a challenge and an active area of research.

This work presents a novel synthesis route for making patchy particles at the sub-micron level that involves the use of capillary condensation. Colloidal silica particles of various sizes were synthesized and ordered into closely-packed arrays via evaporative self-assembly. Various chemical agents were capillary condensed into the voids of this assembly which, due to the face-centered cubic structure of the crystallized colloidal silica, produced distinct "patches" on the particle surface. The patches on these particles were successfully functionalized with gold nanoparticles. This method was shown to provide control over the patch size by modifying the silica particle radius, which thermodynamically changes the amount of capillary condensation. The patchy nature of the resultant particles was confirmed using infrared spectroscopy, scanning electron and optical microscopies, energy dispersive x-ray analysis and zeta potential measurements.

ACKNOWLEDGMENTS

I would like to thank my committee chair, Dr. Nicole Zacharia, and my committee members, Dr. Zhengdong Cheng and Dr. Molly Gentleman, for their guidance and support throughout the course of this research.

Thanks also to my friends and colleagues and the department faculty and staff for making my time at Texas A&M University a great experience. I also want to extend my gratitude to Dr. Nicole Zacharia and the Department of Mechanical Engineering at Texas A&M University for my Graduate Research position, as well as Texas Engineering Experiment Station (TEES) and Texas Water Resources Institute/U.S. Geological Survey (TWRI/USGS) Research Grant for funding this research.

TABLE OF CONTENTS

CHAPTER Page

CHAPTER Page

LIST OF TABLES

LIST OF FIGURES

FIGURE Page

FIGURE Page

FIGURE Page

FIGURE Page

FIGURE Page

FIGURE Page

CHAPTER I

INTRODUCTION

A. Research Significance

Patchy particles have many potential uses in understanding fundamental thermodynamic issues such as the glass transition temperature, gelation, crystallization and novel phase behavior as well as for practical applications. Many of these applications, namely photonics, electronics, enhanced drug delivery and others, stem from the interesting self-assembly of these patchy particles into local and extended ordered superstructures. While theoretical studies are abound on the subject [1], good synthetic methods that will make experimental exploration of patchy particle self-assembly behavior and their consequent use in applications possible are lacking. One of the biggest issues today is the limit of high-yield synthetic methods for patchy particles, especially at the sub-micron scale. In this work, a novel synthesis route for patchy particles using capillary condensation will be discussed, including the ability to modify the "patchiness" of these particles by changing the particle radius.

B. Thesis Outline

Chapter II represents a literature review of Janus particles, which are compartmentalized colloids with 2 different sides of chemistry or polarity. As a subcategory of patchy particles and their predecessor, it is important to discuss them. After a brief introduction, some of the most common syntheses methods, namely the masking/unmasking technique, reactive directional fluxes, microcontact printing, partial contact with a

---

´The journal model is *IEEE Transactions on Automatic Control.*

reactive medium (Pickering emulsion) and electrospraying are considered. Then, several potential applications are discussed, with pertinent examples.

Chapter III represents an extensive literature review on the subject of patchy particles, which are patterned particles with at least one well-defined patch that can have highly directional and strongly anisotropic interactions with other particles or surfaces. They can be regarded as a more generalized Janus particle where the number of patches and their geometry is not limited. After a brief introduction, current syntheses methods will be dicusses in detail, followed by disadvantages and advantages of each method. The main syntheses routes available today encompass templating, colloidal clusters, particle and nanosphere lithographies, glancing angle deposition and capillary fluid flow. Finally, the importance of patchy particles from a fundamental science and application perspective will be discussed.

Chapter IV discusses the novel patchy particle synthetic route developed in this work, using capillary condensation. After an overview of the physics of capillary condensation, the chapter will discuss the procedure used to make patchy particles by this method, with Scanning Electron Microscopy (SEM), Fourier Transform Infrared Spectroscopy (FTIR), Optical Microscopy (OM), Energy-Dispersive X-ray Spectroscopy (EDX) and Zeta Potential used to characterize the patchy particles. The chapter concludes with discussion and recommendations for further research.

Chapter V will focus on the experimental details of all the methods in the previous chapter. Syntheses of all relevant nano- and colloidal particles (ex. silica, gold) will be outlined, as well as experimental details of evaporative self-assembly and capillary condensation, followed by discussion of sample preparation for OM, FTIR, SEM, EDX and Zeta Potential measurements. Finally, Chapter VI will describe some ongoing research projects and the thesis will conclude with a summary in Chapter VII.

CHAPTER II

JANUS PARTICLES

A. Definition

Janus particles are compartmentalized colloids (one of the three states of matter finely dispersed in another, with at least in one dimension in the range from several nm to a few μm) with 2 different sides of chemistry or polarity. Typically, these particles are larger than molecules, but small enough to sustain Brownian motion [2]. The name stems from the Roman God Janus, who is often depicted with two faces. The field has become a very active area of research, which, along with the particle name, has been popularized by Pierre-Gilles de Gennes in his lecture delivered after winning the 1991 Nobel Prize for Physics [3]. Figure 1 [4] shows some of the most common Janus particle architectures in the shapes of spheres, rods and discs. As the figure indicates, functionalization for rods and discs is possible along both the vertical and horizontal axes [5].

B. Synthesis Methods

Figure 2 [6] shows that for even the simple bifunctional spherical Janus particle, there are many methods available for its production. Method (a) shows the masking/demasking technique, which is one the oldest ways to obtain Janus particles. Method (b) shows the use of directional fluxes or fields. In this case the colloidal particle is immobilized on a substrate, and only the exposed face of the particle is functionalized. The second hemisphere is spared the reaction because it is sheltered by the particle itself. This route allows avoiding the tedious masking and unmasking steps. However, this method is generally of low yield as it requires a monolayer

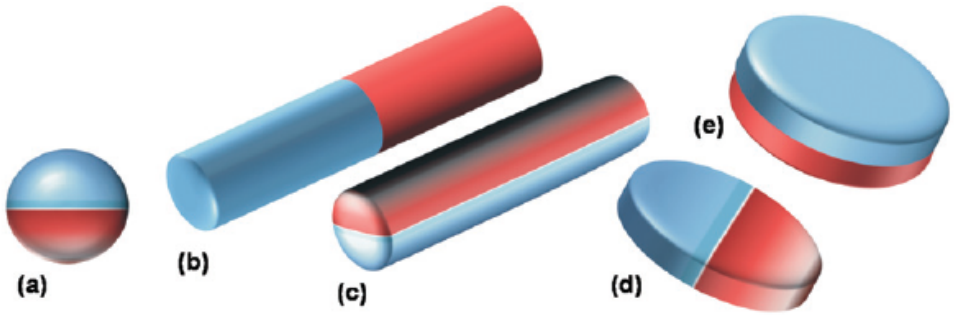

Fig. 1. Possible Janus particle architectures [4], such as (a) sphere, (b,c) cylinders and (d,e) discs.

of spheres, and the quality of the coating deteriorates as the particle size decreases. Method (c) is microcontact printing, where the particle is functionalized by the simultaneous application of pressure on the stamp and the chemical affinity of the transferred groups for the substrate versus the stamp. A commonly used stamp material is PDMS (poly(dimethyl siloxane)). Method (d) describes interfacial and partial contact with a reactive medium, and in this case only the particle area exposed to the reactive medium is functionalized.

Figure 3 [4] provides some particular examples of the methods described in the previous paragraph. Part (a) shows the deposition of particles on a substrate and their functionalization by metal deposition. A common metal of choice is gold. Part (b) shows an ellipsoidal complex core coacervate micelle, which was obtained by the forced coassembly of two block copolymers (poly(ethylene oxide) and polyacrylamide) that each possessed a charged polyelectrolyte segment at one end. The polyelectrolyte ends formed a water-insoluble interpolyelectrolyte complex (IPEC) as a micellar core,

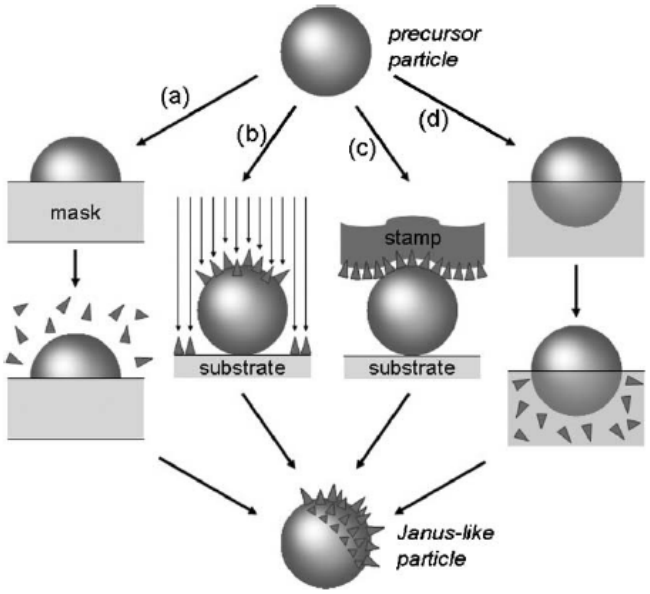

Fig. 2. Four strategies used to modify a Janus particle surface [6]: (a) masking/unmasking, (b) using reactive directional fluxes or fields, (c) microcontact printing and (d) techniques based on interfaces and partial contact with a reactive medium.

and the block segments underwent phase separation. Part (c) is an example of the masking method. In this case, a Pickering emulsion (emulsion stabilized by solid particles) of molten wax and water, and silica particles as stabilizers. The initial solution was created at high temperature, and upon cooling the wax solidified, effectively immobilizing the silica particles and allowing aqueous chemistry to modify the exposed surface. Upon reheating, the Janus particles are released. This method was pioneered by Hong *et al.* [7], which they used to synthesize 800 nm and 1.5 μm silica particles functionalized with various chemistries on one or both sides of the Janus particle. The Janus particle yield is 50% and the solution nature of the method should allow

for an easy scale-up as needed. Part (d) is an example of purely inorganic Janus particles whose formation is assisted by nucleation processes during the growth of the second material or reaction-induced phase separation [4]. Part (e) is an example of microfluidic polymerization. As the scheme indicates, the tip releases a two-phase stream from its top, which is then cut into small particles and solvated by the aqueous phase crossflow containing surfactant coming in from the sides. Photopolymerization locks the shape of the resulting Janus particle. And finally, part (f) demonstrates the use of electrohydrodynamic jetting with a two-phase spinneret tip that can generate spherical and cylindrical Janus particles.

C. Applications

Janus particles are of interest in many areas. For example, Nisisako *et al.* [8] have used electrical anisotropy of Janus particles filled with white and black pigments in their two hemispheres to create a display. The particles were put in a thin layer between two electrodes, and switching the electrical field caused the particles to flip in orientation. They are also of interest in nanomedicine as self-motile, more efficient drug delivery vehicles. An example of such behavior is a biphasic Janus particle with Pt/Polystyrene hemispheres [9], where the catalytic degradation shown in Figure 4 [4] generates an asymmetric distribution of reaction products and an osmotic pressure.

Another area of interest are interesting superstructures. An example can be seen in Figure 5 [10], which shows interesting self-assembled structures displayed by metal-polymer Janus particles. Park *et al.* [10] used rods made up of gold and polypyrrole segments, the self-assembly of which could be tuned between spherical and cylindrical shapes by varying the ratio of the two segments.

Another prominent example is the kinetics of 1 μm fluorescent polystyrene sul-

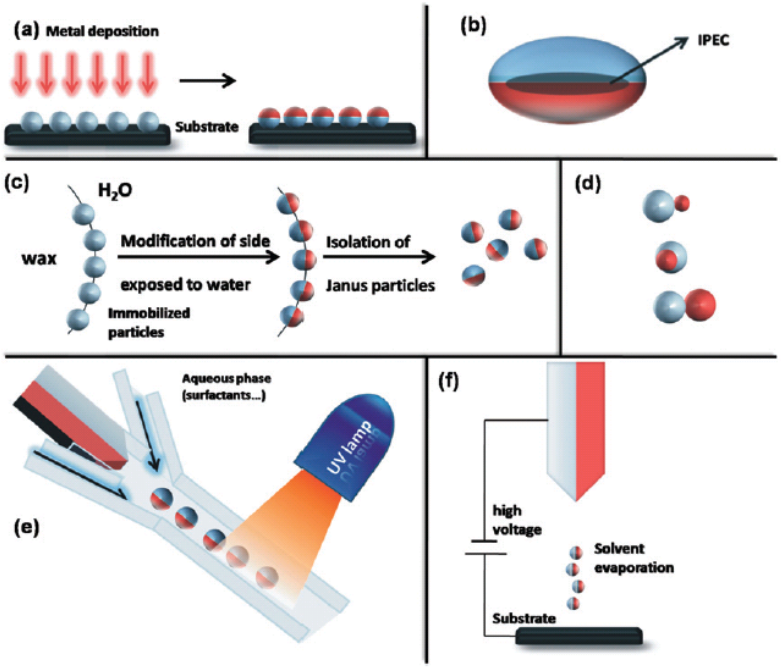

Fig. 3. Janus particle synthesis routes [4]: (a) classical metal deposition, (b) ellipsoidal complex core coacervate micelle, (c) pickering emulsion, (d) snowman-, acorn-, dumbbell-like nanoparticles, (d) microfluidic photopolymerization, and (e) electrospraying.

fate particles, half of which are coated with gold and an aliphatic thiol, as eluciated by Chen *et al.* [11]. Upon addition of salt, electrostatic repulsion from the charged sulfate groups diminishes, and van der Waals forces dominate, causing particle aggregation, as shown in Figure 6, part A. Figure 6, part B shows the multitude of cluster formations observed at 3.8 mM salt concentration over time. Two common clusters observed - capped trigonal bipyramid (CTBP) and octahedron (OCT) clusters - were shown to be at equilibrium with each other, as shown in part C. Part D

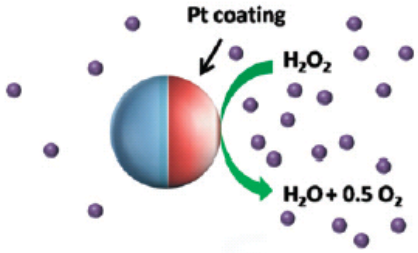

Fig. 4. Self-propulsion of Janus particle via asymmetric distribution of reaction products of the catalytical decomposition of hydrogen peroxide into water and oxygen [4].

is a fluorescence image of the Janus particles forming kinked triple helices.

Finally, Janus particles have a lot of potential as Pickering emulsion stabilizers, from a theoretical and experimental perspective. Unlike small colloidal particles, Janus particles are non-centrosymmetric, and thus possess not only a small surface area, but also amphiphilicity. This explains their remarkably high adsorption strength at interfaces. Binks *et al.* [12] have demonstrated with their theoretical model that a 10 *nm* simple, biphasic Janus particle has 3 times stronger adsorption at the water-oil interface than a homogeneous particle of the same size, at contact angle θ=90°. Figure 7, from a different publication by Binks *et al.* [13], demonstrates the possible contact angles, and the corresponding oil-water boundary shape.

Experimentally, Janus particles have been demonstrated as effective stabilizers. For example, Walther *et al.* [14] have used PMMA/PS (polymethylmethacrylate/polystyrene) Janus particles (Figure 8) to effectively stabilize PMMA/PS blends. As can be seen in the TEM images in Figure 9, increased weight percent of PMMA/PS

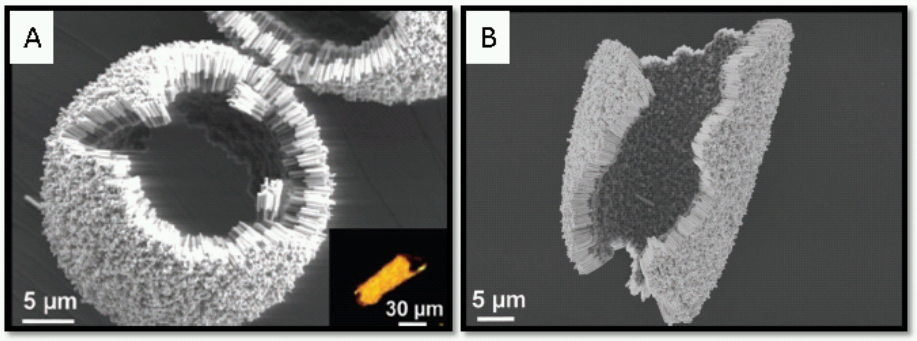

Fig. 5. SEM images of gold-polypyrrole (Au-Ppy) Janus particle aggregates [10]: A - 3:2 Au:Ppy, B - 4:1 Au:Ppy.

Janus particles decreases the size of the PMMA phase, which indicates increased stability of the polymer blend.

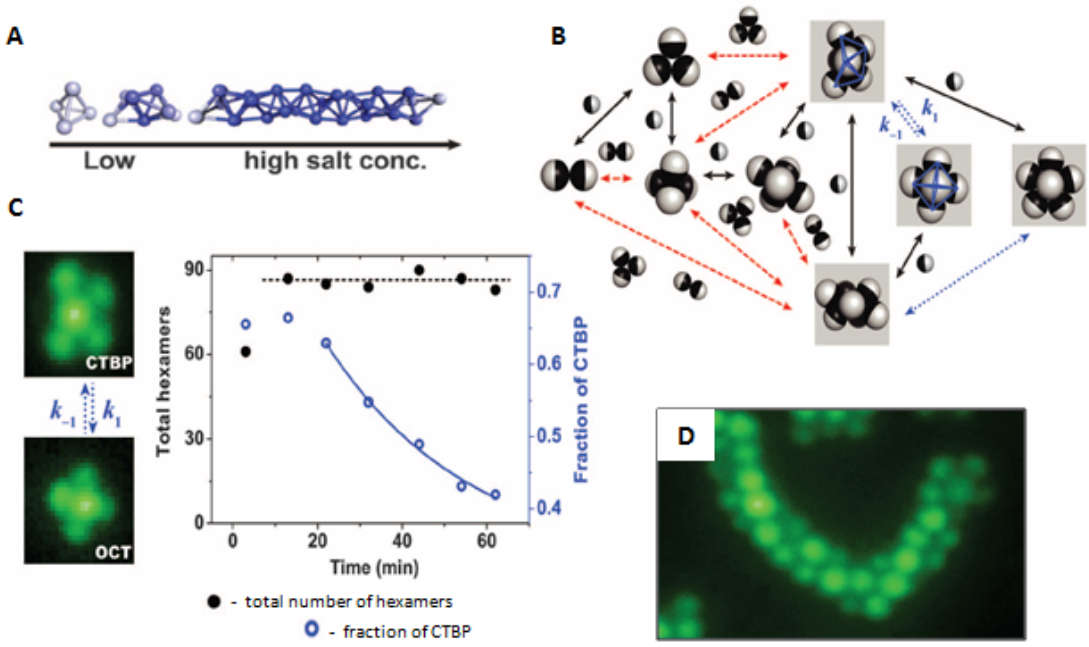

Fig. 6. Janus particle self-assembly [11]: A higher salt concentration causes aggregation due to reduction of electrostatic repulsion forces, B - network of reaction pathways observed for 1 μm particles in experiments at 3.8 mM NaCl, C - kinetics of isomerization between capped trigonal bipyramid (CTBP) and the octahedron (OCT) clusters, D - fluorescence image of a kinked chain.

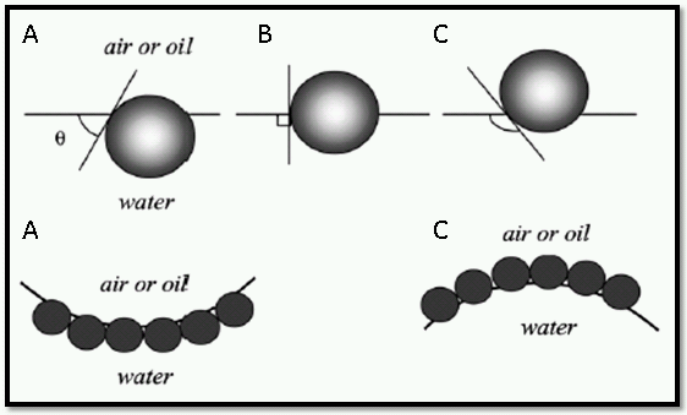

Fig. 7. Contact angle θ, measured in water, of hypothetical spherical particle at the oil and water/air interface, and its respective curvature. A - $\theta < 90°$, hydrophilic particle, B - $\theta = 90°$, Janus particle, C - $\theta > 90°$, hydrophobic particle [13].

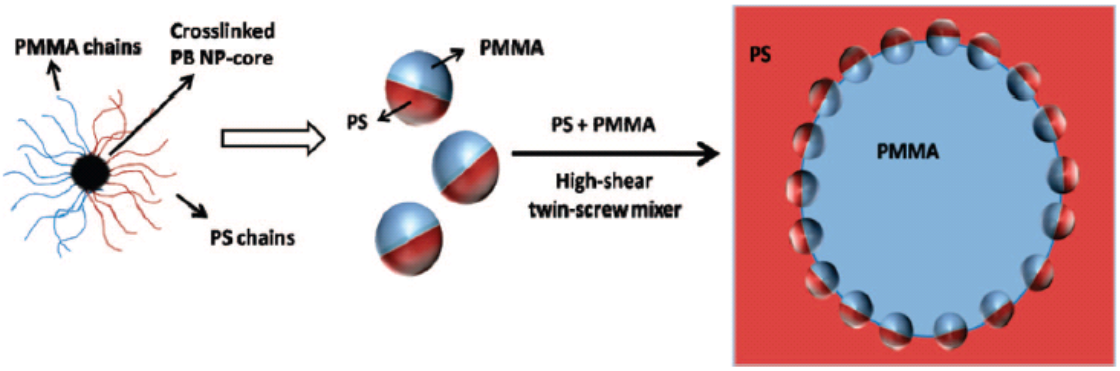

Fig. 8. Structure of PS/PMMA Janus particles and their adsorption at the PS/PMMA blend interface [14].

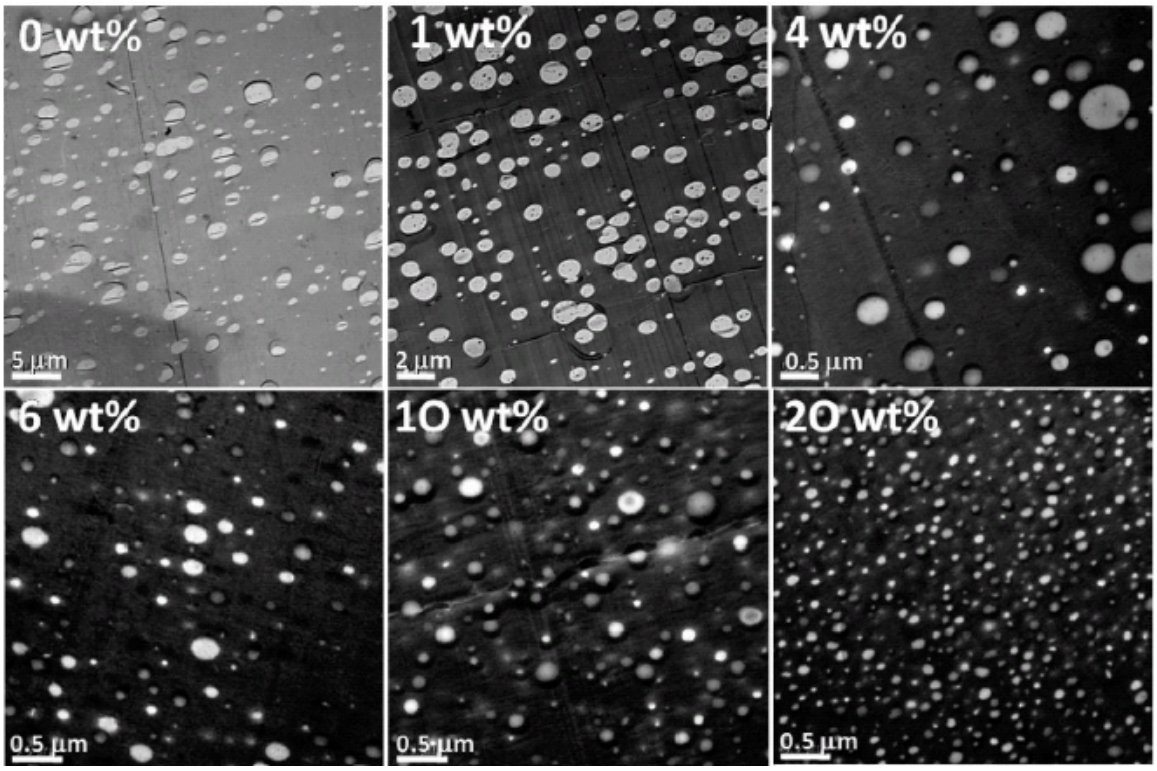

Fig. 9. TEM images of PS/PMMA blend (8:2) with PS/PMMA Janus particles at different weight percentage [14].

CHAPTER III

PATCHY PARTICLES

A. Introduction

Patchy particles are patterned particles with at least one well-defined patch that can have highly directional and strongly anisotropic interactions with other particles or surfaces [15]. This definition also includes biological macromolecules such as globular proteins along with synthetic equivalents of various geometries. Glotzer *et al.* [16] devised a way to categorize patchy particles, as shown in Figure 10. Due to the broad scope of the above definition, this chapter will mostly focus on spherical patchy particles.

B. Synthesis Methods

Various synthesis routes exist for patchy particles. As with Janus particles, the biggest problem is the lack of synthetic methods for small particles below 0.5 μm as well as getting a significantly high yield that will allow for efficient use in applications. Described below are six of the most common methods currently employed.

1. Templating

Templating typically involves 3 steps:

1. Partial coverage, or masking, of the particle surface.
2. Chemical modification of remaining unmasked particle surface.
3. Remove the template.

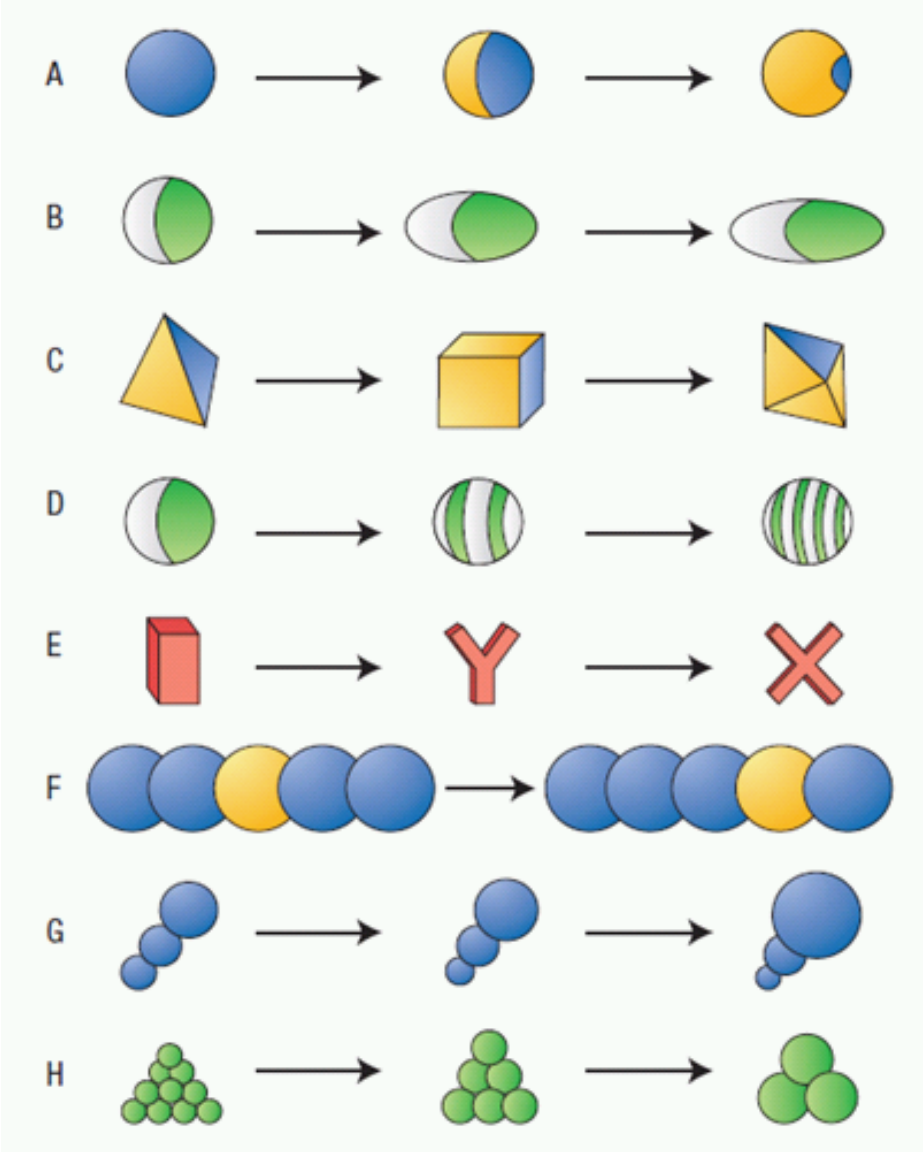

Fig. 10. Anisotropy dimensions of patchy particles: A - surface coverage (patchiness), B - aspect ratio, C - faceting, D - pattern quantization, E - branching, F - chemical ordering, G - shape gradient, H - roughness [16].

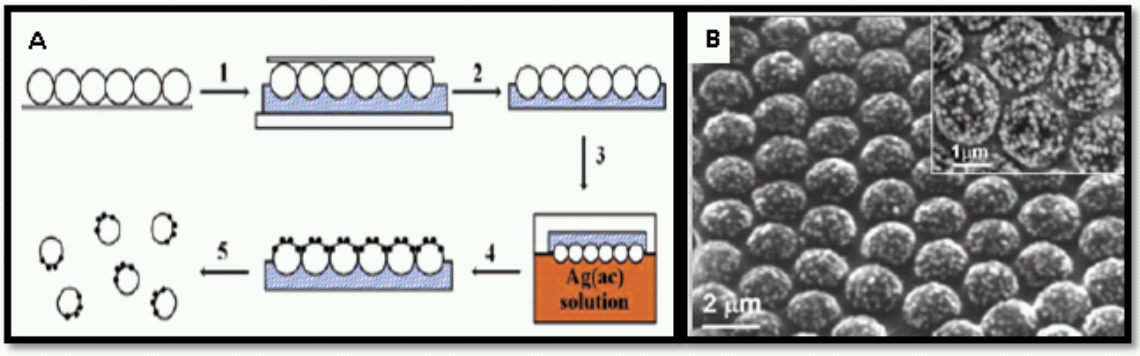

Fig. 11. Sulfate-terminated polystyrene particles with silver coating made by templating: A - synthesis route for making particles involving a PDMS stamp and electroless deposition of silver, B - SEM image of a sulfate-terminated polystyrene spheres after electroless silver deposition [18].

This is very similar to the masking/unmasking technique shown in Figure 2, except in this case the template is not limited to covering half of the particle's surface. Partial coverage has been achieved employing various combinations of phases, including the air-solid, air-liquid, liquid-liquid and liquid-solid interfaces [17]. The contact angle of the particle with the "mask" of choice can be controlled by the addition of surface-active agents to any of the reaction phases involved, or chemically attaching them to the particle surface directly.

Cui and Kretzschmar [18] made sulfate-terminated polystyrene (sPS) particles that are partially covered in silver patches, as shown in Figure 11. Part A of Figure 11 schematically describes the synthesis. A monolayer of sPS spheres formed on silicon wafer is pressed into a pre-cured poly(dimethylsiloxane) (PDMS) mask (step 1). Once the PDMS stamp is fully cured, it is peeled off from the silicon wafer to produce sPS spheres immobilized in the stamp (step 2). Silver nanoparticles are then formed on

the exposed PS particle surface by immersing the PDMS-sPS assembly in a solution of silver acetate and formaldehyde under basic conditions (steps 3 and 4). Finally, the PDMS template is removed to release the sPS particles with silver patches (step 5). An SEM image of the particles can be seen in part B of Figure 11, where the 2.4 μm sPS particles are covered with 150-200 nm silver patches.

Another example of templating is using wax-in-water emulsions to make patchy particles. Perro *et al.* [19] modified the penetration of silica particles into molten wax by making their surface increasingly hydrophobic with addition of a surfactant, cetyltrimethylammonium bromide (CTAB). Once the wax cooled down and solidifed, the exposed silica surface was reacted with 3-aminopropyltriethoxysilane, followed by attaching gold nanoparticles to the pendant amine groups. Figure 12 [19] shows 800 nm silica particles with increasing surfactant concentration going left to right. Increasing the concentration of CTAB increases the contact angle of silica, resulting in less exposed silica surface that can be chemically modified and then reacted with gold.

Rastogi *et al.* [20] were able to make magnetic, patchy colloidal particles using droplet templating on a superhydrophobic substrate. 5.0 μL droplets containing 1000 nm latex microparticles and 180 nm magnetic (Fe55/Ni45) nanoparticles dispersed in water were placed onto a superhydrophobic substrate. As the water evaporated, resulting in compaction and solidification of the particles, the application of a non-uniform magnetic field caused the Fe/Ni nanoparticles to aggregate in particular regions and form patches, as can be seen in Figure 13. Desired magnetic fields were generated by placing rod-like magnets in particular geometries (Figure 13, right section).

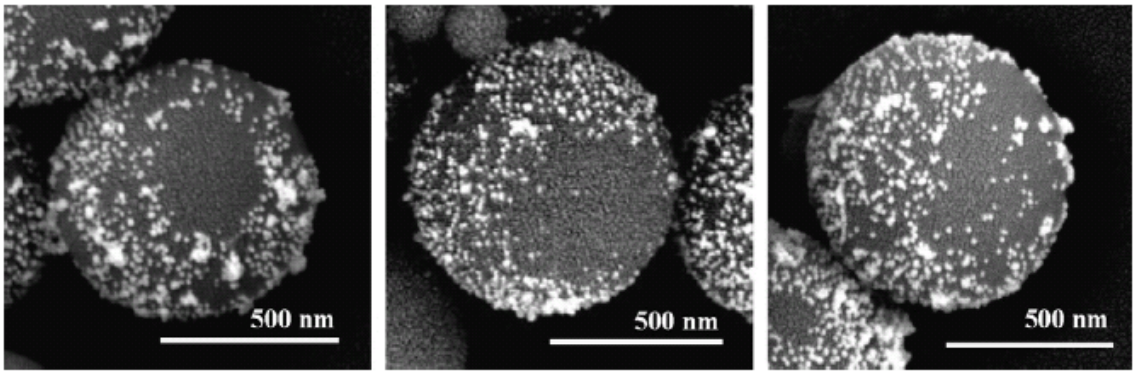

Fig. 12. 800 *nm* silica particles functionalized with 3-aminopropyltriethoxy silane and gold nanoparticles. From left to right, the ratio of CTAB concentration to silica surface is tuned from 2.5×10^{-6} mol/Lm^2 to 5×10^{-6} mol/Lm^2 [19].

2. Colloidal Clusters

This method was pioneered by Manoharan *et al.* [21], who packed 844 *nm* sulfate-terminated polystyrene spheres (sPs) into various clusters. They made a Pickering toluene-in-water emulsion with lightly cross-linked sPs particles at the solvent interface, and by controlling the rate of toluene evaporation, sPs clusters of various geometries were observed, as shown in Figure 14. Once most of the toluene evaporates, and the sPs particles in a given emulsion droplet begin to touch one another, further evaporation leads to strong capillary forces which quickly rearrange the particles. Upon full toluene evaporation, the sPs particles de-swell (toluene is a favorable solvent for polystyrene) and the resultant van der Vaals forces keep the particles in place. Moreover, the remaining aqueous atmosphere charges the pendant sulfate groups, which keeps the clusters from aggregating any further.

Cho *et al.* [22] were then able to extend the above method to include bidisperse

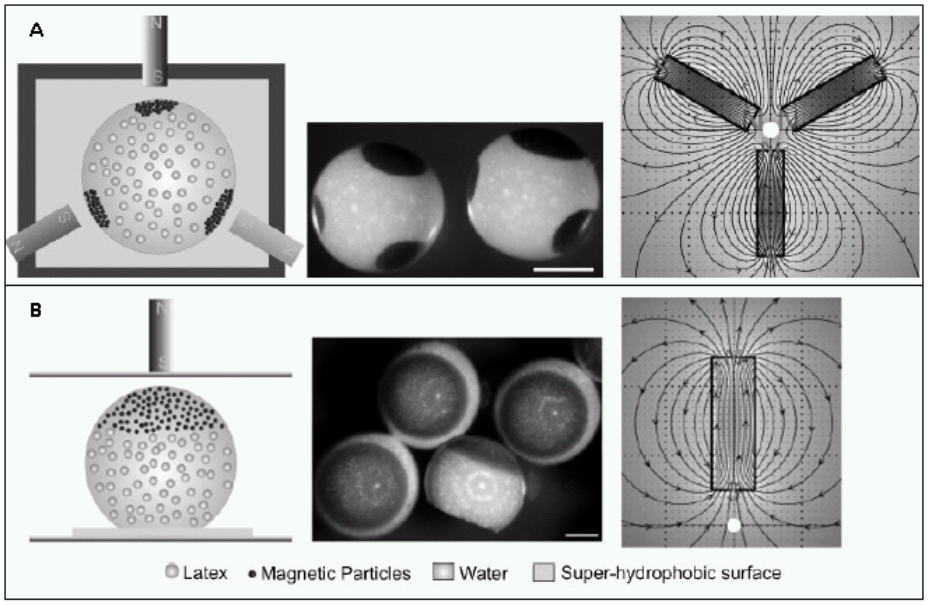

Fig. 13. From left to right, the assembly configuration, SEM image and simulation pattern of applied external magnetic field for: A - tri-patch magnetic supraparticles, B - single patch magnetic supraparticles [20]. Scale bar = 500 μm.

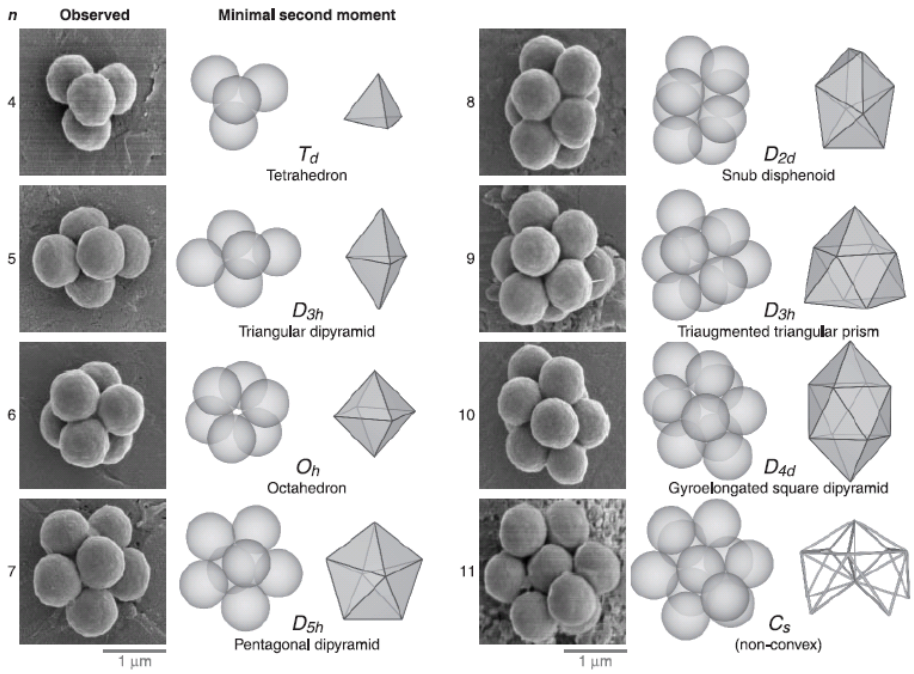

Fig. 14. Various colloidal clusters observed for 844 *nm* sPs: left column - SEM images of various clusters, middle column - numerical simulations obtained by minimizing the total surface energy of the clusers, right column - polyhedra formed by connecting neighboring particle centers with straight lines [21].

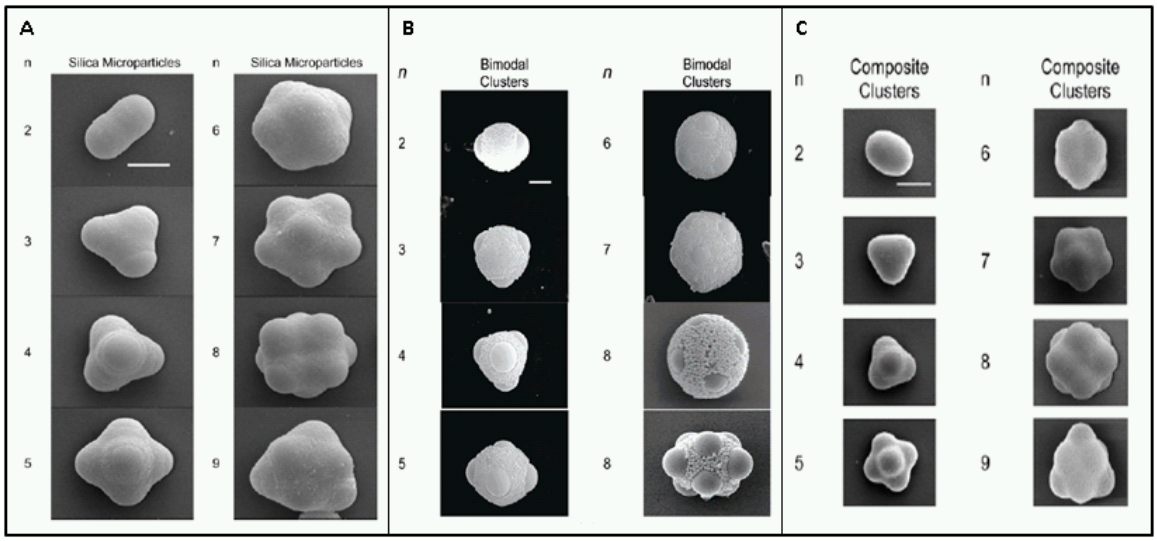

Fig. 15. Colloidal clusters observed for bidisperse mixtures of silica and amidine polystyrene particles: A - silica particles, 800 nm and 12 nm, B - silica particles, 2300 nm and 230 nm, C - amidine polystyrene (1000 nm) and silica (30 nm) [22].

particles of silica, as well as mixing silica, amidine polystyrene and titania of various sizes to form colloidal clusters. Figure 15 shows some of the colloidal clusters formed using various sizes, particle types and ratios between the bidisperse particles in each assembly. A water-in-oil emulsion was used, and as can be seen by comparing Figure 14 and 15, the colloidal clusters formed are similar, but in the case of bidisperse clusters, the arrangement of small particles is determined by the interparticle interactions.

Another method involves creating colloidal assemblies by trapping particles in confined geometries using microfluidics, shown in Figure 16. The ordering (F) and roughness (H) anisotropy dimensions, as seen in Figure 10 [23], can be tuned using

this method. The general methodology, as reported by Sung *et al.* [23], involves packing precursor 21.1 μm polystyrene particles into a narrow terminal channel with a combination of confinement effects and microfluidics. The final step is to permanently fix the structure in place by thermally fusing the particles. Patchy particles with alternating bond angles, uniform roughness and varying patch configurations can be made using this method.

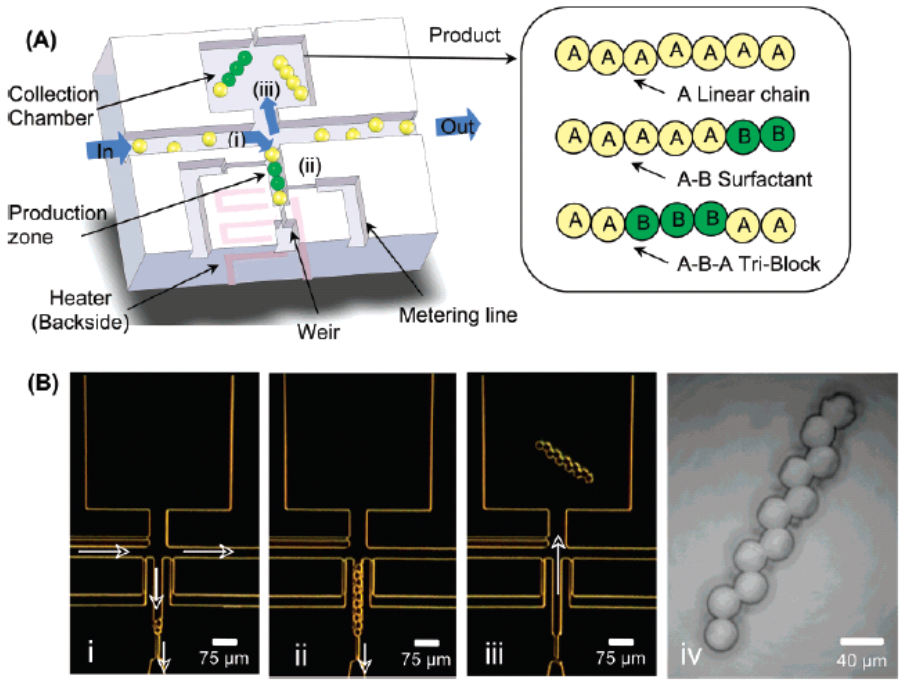

Fig. 16. A - schematic of a microfluidic device used to make colloidal clusters by Sung *et al.* [23] B - reaction schematic where (i) particles flow into production zone (ii) their sequence is solidified via thermal fusion at 80^oC and (iii) they are released and collected. An optical microscope image of an examplary particle is shown in (iv) [23].

Colloidal assemblies are an attractive method because it is scalable and relatively

large volumes can be synthesized. It is also quite versatile since various particle size combinations produce many different particle geometries by combining the branching (E) and roughness (H) anisotropy dimensions, as described in Figure 10. However, it is difficult to control the number of particles per emulsion droplet, and thus there is a distribution of colloidal clusters in every synthesis.

3. Particle Lithography

Particle Lithography involves attaching smaller particles to a larger particle, where the surface of the latter is partly masked. This process, first developed by Snyder *et al.* [24], is shown in Figure 17, part A. Typically, the larger particle is attached to a surface of opposite charge via electrostatic attraction, and this surface then acts as a mask. In this specific example, a cationic amidine polystyrene sphere is attached to a negatively-charged glass slide. Next, poly(styrene sulfonate) with R_g = 10 nm is attached to the exposed surface of the amidine polystyrene particle, rendering the surface negatively charged, save for the masked region. Finally, the assembly is sonicated off the glass slide and an anionic particle can be attached to the positively charged unmasked region of the assembly. Figure 17, part B shows an optical microscope image of 1.5 μm amidine polystyrene particle and 2.4 μm sulfate polystyrene particles forming colloidal doublets.

This type of particle lithography can be extended to more than one particle layer. For example, Yake *et al.* [25] have fabricated particles with two layers of patterning, as shown in figure 18. In this case, after one layer of particles has been adsorbed onto the larger sphere, a cationic polyelectrolyte is adsorbed to the anionic coating particles, and the adsorption cycle can now be repeated for additional anionic particles, of the same or larger size. Figure 18, part B shows a typical particle made using this method. Specifically, the base particle is a 1 μm amine-functionalized silica particle,

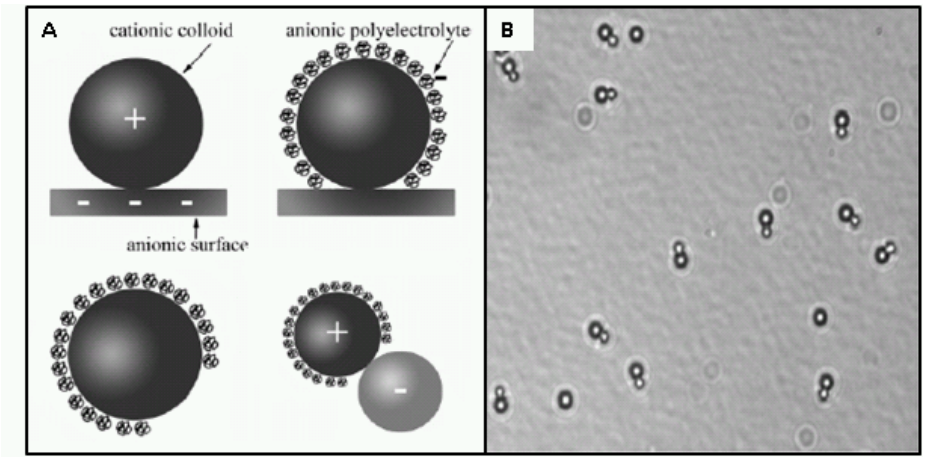

Fig. 17. A - schematic of the particle lithography method [24]. Positively charged base particle adsorbs to a negatively charged glass slide in water, followed by deposition of negatively-charged particles to the base particle. The final assembly is sonicated off the substrate and attached to another negative particle using the bare, unmasked portion of the base particle, B - optical microscope image of an exemplary colloidal doublet [24].

coated with 20 nm sulfated polystyrene particles, followed by a monolayer of poly(allyl amine hydrochloride) or PAH, and finally 84 nm sulfate polystyrene particles. The size of the lithographed region is controlled by varying the particle size, the radius of gyration, and the Debye length of the polyelectrolyte. The lithographed region is also a function of the radius of the main particle (a) and the coating particle (R), as shown in Figure 18, part C. Simple geometry shows that the diameter of the lithographed region (D) is:

$$D = 4\sqrt{aR}$$

This method has allowed Snyder *et al.* [26] to assemble three colloidal particles with

similar bond angles to that of a water molecule.

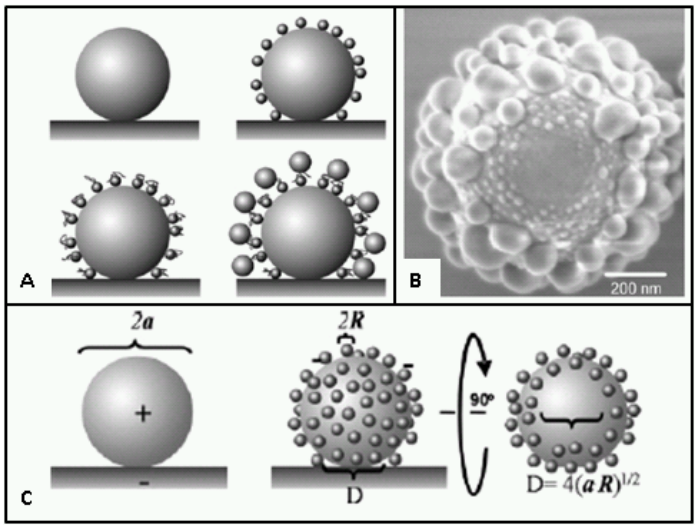

Fig. 18. Complex particle lithography: A - the top two panels are summarized in Figure 17, part A, with the bottom two panels showing the additional steps of cationic polyelectrolyte adsorption, topped with another layer of anionic particles of the same or different size, B - SEM of an exemplary patchy particle, C - relationship between base particle radius (a), coating particle radius (R) and the diameter of the lithographed region (D) [25].

Particle lithography allows the making of very complex structures, based on the geometry and size of the particles adsorbed to the base particle. However, this method is based on the functionalization of individual particles and is thus difficult to scale-up in terms of production volume and synthesis time.

4. Glancing Angle Deposition

As mentioned in Chapter II and shown in Figure 2 (part b) and Figure 3 (part a), vapor deposition done vertically on a monolayer of particles produces Janus particles.

However, if the angle of deposition is changed, the resultant metal patches no longer cover exactly half of the particle. When the vapor deposition is performed at an inclined angle with respect to the plane defined by the monolayer, the technique is called glancing-angle deposition (GLAD) [17], and is represented in Figure 19. Here, a monolayer of spheres on a substrate is exposed to a metal vapor at varying angles of evaporation θ.

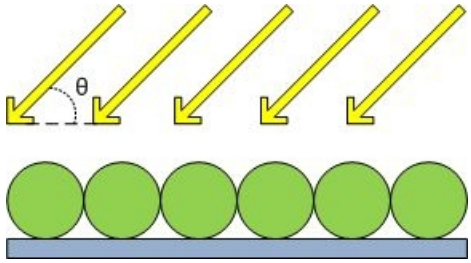

Fig. 19. Particles on a substrate undergoing glancing angle deposition. θ is the angle of incidence of the metal vapor.

Unlike in the case of Janus particle, the shadow mask during metal deposition is not only the particle itself, but also the neighboring particles in the 2 dimensional close-packed particle array. The geometry of the patch depends on two variables: the angle of evaporation θ and the monolayer orientation relative to the evaporation source θ [17]. This can be clearly visualized in Figure 20, where Pawar *et al.* [27] vary α from 0° to 40° while θ=10°. The bottom images are results predicted by computational modeling. A single GLAD deposition can produce partches covering 3.7-50% of the particle surface area [27].

The GLAD technique can also be used to deposit multiple patches at different angles. Unlike a single deposition, multiple evaporation sources and multiple evap-

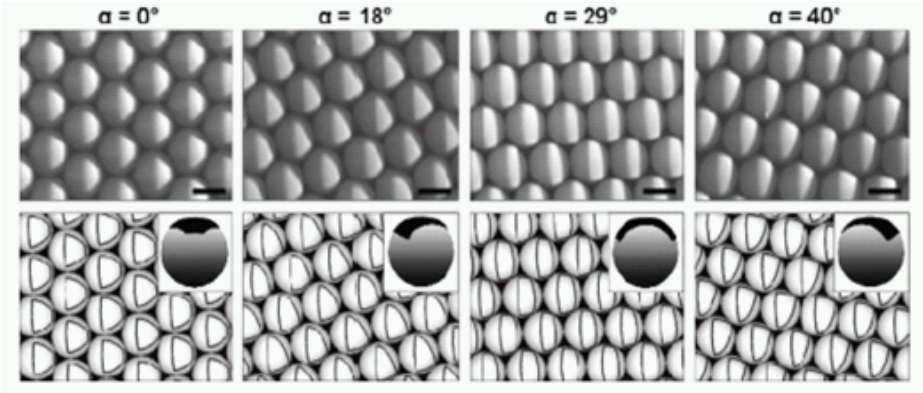

Fig. 20. Experimental (top) and calculated (bottom) gold patches on 2.4 μm sulfated polystyrene particles as a function of monolayer orientation α for the angle of incidence $\theta = 10°$ [27]. Scale bar = 2 μm.

orations onto the same sample can produce overlapping patches of more complex geometries, and they can lead to patches as small as 1.6% of the particle surface area [28]. Figure 21 [28] shows a sample particle deposited with two deposition at $\xi = 60°$, where ξ represents the angle between the two depositions. In part A, the top view of particle monolayer during sequential vapor depositions at $\theta = 5°$, $\alpha = 30°$ is shown. Blue and red arrows represent the direction of vapor deposition; in this case Au metal was used for both depositions. The gray spheres provide the shadowing effect to the patchy particle which determine the patch geometry at these particular deposition conditions. In part B, SEM is used to confirm the patchy nature of the particles, with a mathematical model of the resultant particle with these deposition conditions in the inset. For this experiment, Pawar *et al.* [28] used 2.4 μm sulfate polystyrene particles.

It is also possible to create multiple simple or complex patches on one particle.

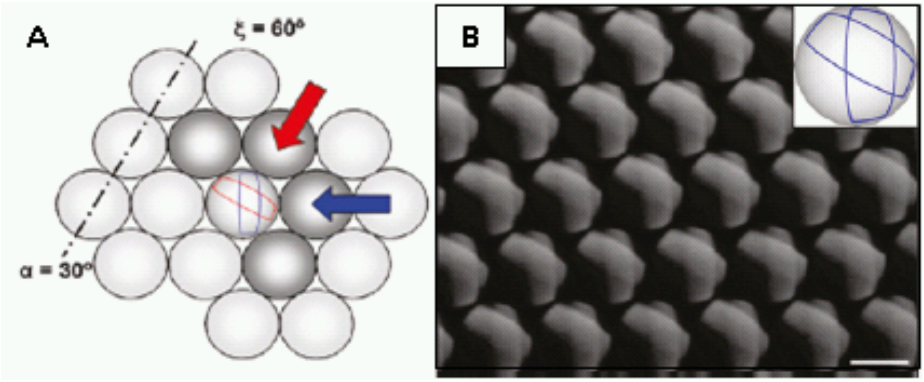

Fig. 21. A - top view of particle monolayer during sequential vapor depositions at $\xi = 60°$, $\theta = 5°$, $\alpha = 30°$ [28]. Blue and red arrows represent the direction of vapor deposition. Gray spheres are associated with the shadowing effect. B - SEM images obtained by sequential vapor deposition at angle $\xi = 60°$ between vapor depositions [28]. Multifunctional patchy particles with Au patches with $\theta = 10°$, $\alpha = 30°$ is obtained. Inset - patch geometry obtained with mathematical models. Scale bar = 2 μm.

By combining GLAD with PDMS stamping, Pawar *et al.* [28] were able to make two patches on one particle, shown in Figure 22 [28]. Part A shows all the steps involved, namely deposition of the first patch, followed by PDMS stamping, which effectively removes the particles from the substrate and exposes the unmodified surface, onto which a second vapor deposition can be performed. Upon sonication, a 2.5 μm PS particle with two patches, with each patch covering 25% of the particle surface, can be produced, as observed via SEM in part B.

The advantage of the GLAD technique is good control of patch size and geometry, and the ability to create multiple patches on one particle by combining GLAD and PDMS-stamping. In addition, different metals can be deposited which can be used

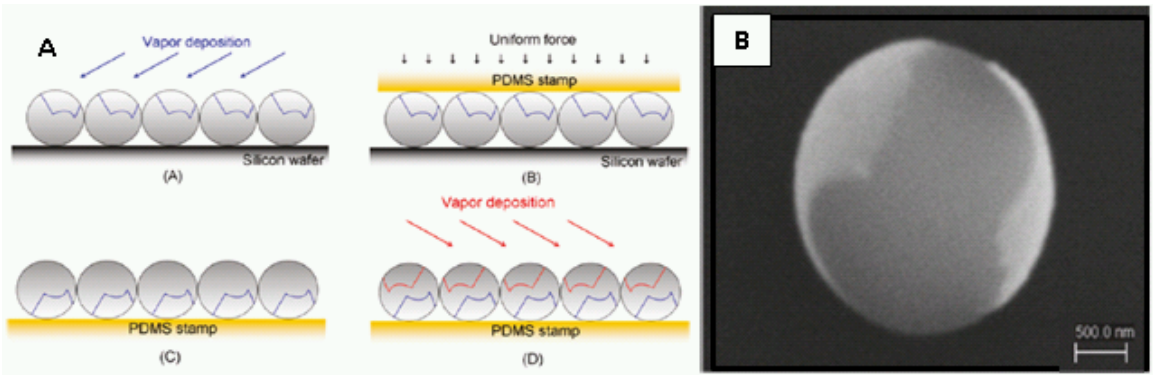

Fig. 22. Multiple patches on a particle using PDMS stamping: A - (A) make first patch using GLAD on a close-packed monolayer of particles, (B) stamp with PDMS, (C) remove from initial substrate to expose unstamped surface and (D) perform another GLAD deposition, B - SEM image of representative particle [28].

to create alloys, increasing the dimensions of branching (E) and chemical ordering (F) [17], as shown in Figure 19. Disadvantages include low yield of patchy particles since only a monolayer of particles over a relatively small area can be functionalized per deposition. Another issue are defects in the closed-packed particle assembly, which can lead to different patches within one batch, but especially between batches.

5. Nanosphere Lithography

Nanosphere lithography involves a three dimensional close-packed array of particles, where the top layer of particles is used as a mask to determine the pattern of deposited metal on the lower layer(s). Figure 23 [29] shows 3 layers of a hexagonally packed close array of particle with the (1 1 1) plane parallel to the substrate. The 3-dimensional packing structure as well as the substrate and metal evaporation angles all determine

the final pattern on the patchy particles, and thus no extrinsic mask is required. To reveal the patchy particles, the layer(s) of colloidal particle used as a mask must be selectively removed. This is typically [29] accomplished by placing double sided adhesive tape on the metal coated surface of the colloidal crystal and covering with a glass slide on top of the tape. After applying 0.2 kg/cm^2 pressure for 10 minutes, the glass slide can be peeled off along with the adhesive tape and the top monolayer of the colloidal assembly. Figure 24 shows some of the possible patchy particles that can be obtained using this method. Zhang *et al.* [29] used 925 nm polystyrene spheres, packed into close-packed arrays by withdrawing a charged substrate from a colloidal dispersion. The crystal facets of the top monolayer were varied to produce different gold patterns. In addition, it is possible to create patchy particles using reactive ion etching, with sp, sp^2 and sp^3 geometries of the patches [30].

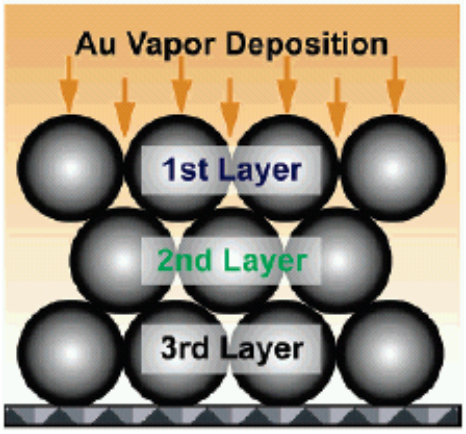

Fig. 23. Nanosphere lithography schematic: hexagonally close-packed 3D array of spheres with (111) facets parallel to substrate, where the top two layers are used as masks to create metal patches on the layer below [29].

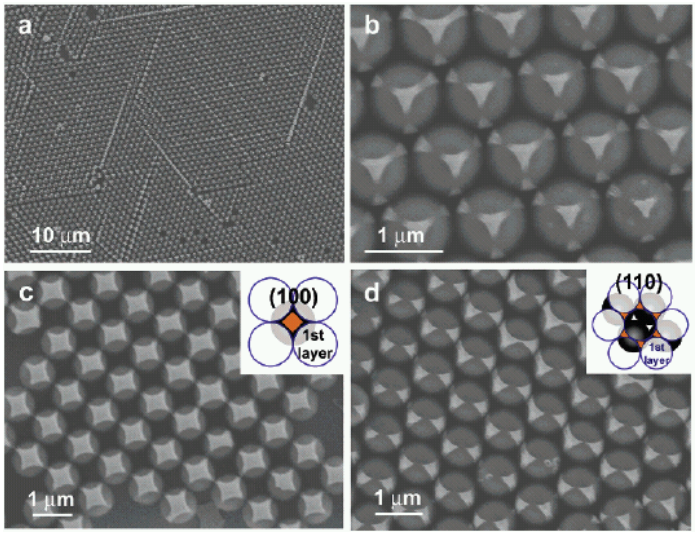

Fig. 24. SEM images of Au-patterned (bright spots) 925 *nm* polystyrene spheres with Au patterns where the top monolayer is used as mask, with different facets parallel to substrate for top monolayer: (a) low and (b) high magnification SEM images with (111) facet, (c) (100) and (d) (110) facets [29]. Inset in (c) and (d) shows schematic of expected pattern.

An advantage of this technique is the ability to create patterns that are as small the particles used to create them, effectively lowering the resolution of created patterns. However, one must be careful to separate the different layers of the modified close-packed assembly as each layer has different patch sizes and geometry, and this is somewhat difficult to achieve practically. And as with the GLAD method, any defects in the close-packed assembly or in the number of layers changes the geometry of the patch.

6. Capillary Fluid Flow

a. Microfluidics

For polymeric particles there are two main possibilities in terms of microfluidic devices: emulsification and continuous flow projection photolithography [31]. Emulsification involves using liquid monomers with an immiscible fluid which acts as an emulsifier, after which the monomer droplets are polymerized (depending on the polymer, polymerization can be thermally- or photo-induced). Emulsification can be further subdivided into microchannel-based and capillary-based microsystems. Continuous flow projection photolithography is a direct polymerization technique where the polymer solution is irradiated with UV light through an optical microscope objective while it is flowing in a microchannel. Typical particle sizes possible with these method range between 40 and 100 μm [17]. In the case of a polymerizable liquid, the resultant di- or tri- phasic droplets can be cured by thermally- or photo-induced polymerization [31]. Capillary fluid flow has been used to achieve Janus, multi-phasic, coreshell, and porous particles [31]. For example, Bong *et al.* [32] have used various microfluidic devices to achieve different patchy particle geometries, as seen in Figure 25 [32], in a method they call hydrodynamic focusing lithography (HFL). The microfluidic devices consist of gas permeable two-layered PDMS channels. Poly(ethylene glycol) diacrylate (PEGDA) monomer with Darocur 1173 initiator and a fluorescent dye (100 nm blue fluorescent beads, 200 nm green fluorescent beads or rhodamine A) are introduced into a common microchannel from side-channels with varying geometry (Figure 25, parts A and C). The flow rate, side-channel dimensions and UV mask geometry control the size of the particles and the patches on them. Triangular and cross UV masks produced triangular- and cross-shaped tri-phasic particles, as shown in Figure 25, part B and D, respectively.

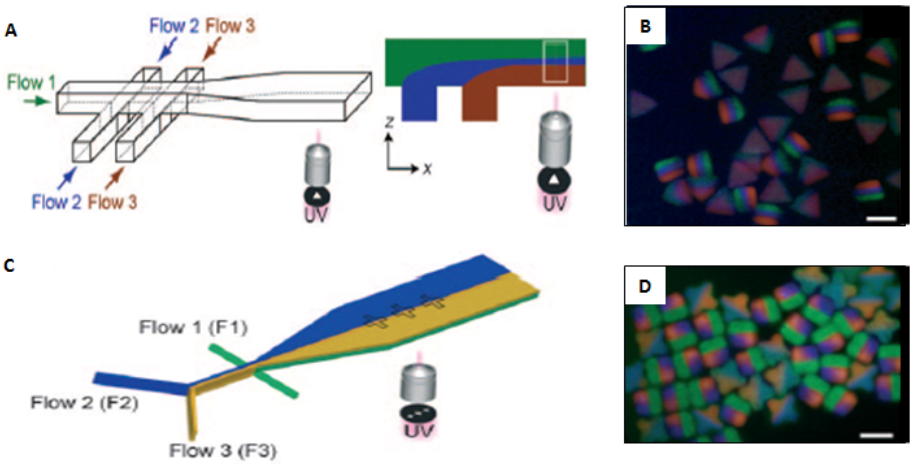

Fig. 25. Schematic patchy particles via microfluidics: A,C - microfluidic devices for triphasic particles. Flow 1, 2 and 3 are PEGDA with 200 nm green fluorescent beads, 100 nm blue fluorescent beads and PEGDA with rhodamine A, respectively, B,D - fluorescent images of triphasic particles produced by A and C, respectively [32]. Scale bar = 40 μm (A) and 30 μm (B).

b. Electrohydrodynamic Jetting

When an electrical field is applied to a liquid, the portion of liquid at the nozzle (see Figure 26, part A,B [33]) transforms into a Taylor cone [34]. Above this threshold voltage the liquid is then ejected, and if said liquid contains a monomer and solvent, the rapid evaporation of the solvent and simultaneous polymerization of the monomer leads to formation of a solid. Depending on the viscosity, conductivity and surface tension of the liquid, as well as applied electrical field and rate of liquid flow, the resultant solid varies in geometry from elongated fibers to small particles. Roh *et al.* [33] used this technique to make tri-phasic particles, shown in Figure 26 [33]. By using a side-by-side needle configuration, it is possible to introduce different polymer

solutions simultaneously while maintaining laminar flow.

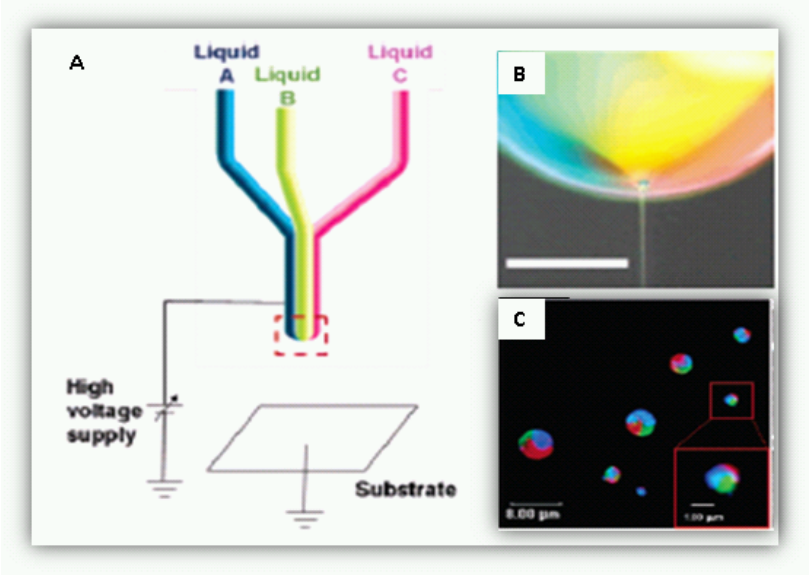

Fig. 26. A - typical electrified jetting setup with triple side-by-side capillaries, B - close-up photograph of jet ejection point of the capillary outlet region (scale bar = 500 μm, C - confocal microscope images for patchy particles made of P(AAm-co-AA) and PAA; individual phases labelled with FITC (blue), Rhodamine B (green) and Alexa Fluor 647 (red) (scale bar = 8 μm) [33].

c. Advantages and Disadvantages

Due to the continuous nature of this synthesis method, it is very easy to scale up this method for high yield patchy particle production. Both electrohydrodynamic jetting and microfluidics can be used to create complicated particle shapes with varying patch sizes. For electrohydronamic jetting, the narrowest particle size distribution is typicaly 15% [17], which can be a problem with applications such as self-assembly or photonics. Additionally, this method is better suited for water-soluble polymers,

which limits starting materials [17]. Unfortunately, it cannot be used to make particles smaller than 40 μm.

C. Applications

Anisotropic properties and the assembly of "patchy" particles are potentially powerful tools for the bottom-up assembly of complex materials as well as for the creation of unusual or previously unobserved phases. These materials may have new or improved electronic, optical, or other types of properties such as novel phase behaviour in solution.

Patchy particle potential applications include:

1. photonic crystals [35]
2. targeted drug delivery [36]
3. electronics [37]

All of the applications and fundamental scientific study relies on the self-assembly of patchy particles into complicated structures. In terms of fundamental science, patchy particles can help address self assembly, at the well-defined, local level or as extended structures, as well as gelation (dynamical arrest at low concentration) [1]. Interactions between anisotropic particles can be used to approximate directional bonding in polar molecules. For the latter, it is possible to observe gel formation without adventitious macroscopic condensation and to supress the liquid-gas separation [1]. Other fundamental issues that can be addressed include the thermodynamics behind condensed matter such as crystallization and glass transition. Moreover, colloidal particle behavior can be compared to entities on the atomic scale since they can

both undergo Brownian motion. Thus, van der Waals forces, electrostatic, steric repulsive forces, and dipolar interactions influence colloidal particles in a similar fashion to those of atoms and molecules [38].

Patchy particles are important for drug-delivery purposes for several reasons [39]. For example, drug delivery carrier shapes have a direct impact on their susceptibility to uptake by immune cells. The degradation of the particle itself and the rate of drug release from the carrier is also a shape-sensitive process. Decuzzia *et al.* [40] have compared the effect of particle volume and shape on adhesive strength and drug release. They found that nonspherical particles with flat faces will have zero-order release while particles of varying thickness offer unique drug release rate as the particle changes shape with time, especially in prescence of flow. The ability to label drug carriers with magnetic, radioisotopic, bioluminescent and fluorescent patches is also of interest since it will allow effective tracking of the drug carrier, which is especially important for certain applications such as cancer tumor targeting and in-vivo studies.

The nanostructuring of the semiconductor introduces profound changes in its photoelectrochemical properties. Mesoporous oxide films are composed of nanometer-sized crystal arrays, from oxides such as TiO_2, ZnO, SnO_2 and Nb_2O_5, or chalcogenides such as CdSe [37]. These arrays are interconneted which allows electronic conduction to take place. Although still of lower efficiency, the nanostructured cells have advantages over conventional solar cells, such as the ability to capture light from all angles, for example. The ability to produce patchy particles that will readily form 3-dimensional structures will move the field closer towards real-world applications.

Photonic crystals are materials that have a periodic refractive index that promotes an optical band gap [35]. While there are plenty of symmetrical and homogeneous materials that can be used to create photonic band-gap materials (face-centered cubic arrays of colloidal silica spheres is a good example), a crystal lattice composed

of nonspherical base units has been shown to promote large photonic band gaps; the assembly is also less susceptible to the defects, which have fatal consequences for bandgap materials, that can occur during colloidal self-assembly [35]. Patchy particles can be made in non-symmetrical shape, and the nature of their patch could create some very interesting self-assembled superstructures for enhanced optical materials.

CHAPTER IV

PATCHY PARTICLE VIA CAPILLARY CONDENSATION

A. Capillary Condensation

The pressure difference across a curved interface can be described by the Young-Laplace equation:

$$\Delta p = \gamma(\frac{1}{R_1} + \frac{1}{R_2}) \tag{4.1}$$

where

Δp	=	Pressure difference across curved interface
γ	=	Surface tension
R_1 and R_2	=	Radii of curvature of any two normal sections of the surface perpendicular to one another

For some common specific surfaces, the Young-Laplace equation becomes:

1. For a spherical surface, R_1=R_2=R

$$\Delta p = \frac{2\gamma}{R} \tag{4.2}$$

2. For a cylindrical surface, $R_1 \to \infty$

$$\Delta p = \frac{\gamma}{R} \tag{4.3}$$

3. For a planar surface, $R_1 = R_2 \to \infty$

$$\Delta p = 0 \tag{4.4}$$

For very small particles, the pressure difference across a curved interface may be so large as to change the chemical potential of a given material. For example, for a spherical droplet of 50 nm and a surface tension of 80 mN/m, the pressure difference across the interface has a magnitude of $3.2 \times 10^6 Pa$ or ≈ 32 atm.

While the Laplace equation is used to calculate the pressure difference across an interface, the Kelvin equation can be used to evaluate the actual pressure above a given surface. The Kelvin equation can be applied to both liquid drops (positive mean radius of curvature) and to bubbles and capillary-condensed liquid (negative mean radius of curvature). The general form of the Kelvin equation is shown in equation (4.5) below:

$$RTln(\frac{P}{P_o}) = \frac{2\gamma V_m}{R_s} \tag{4.5}$$

where

R = Universal gas constant

T = Temperature

P = Pressure

P_o = Standard vapor pressure

γ = Surface tension at the liquid-vapor interface

V_m = Molar volume of the liquid

R_s = Radius of spherical drop

Back in 1979, Israelachvili and Fischer [41] verified experimentally the validity of the Kelvin equation for capillary condensation via multiple beam interferometry. The

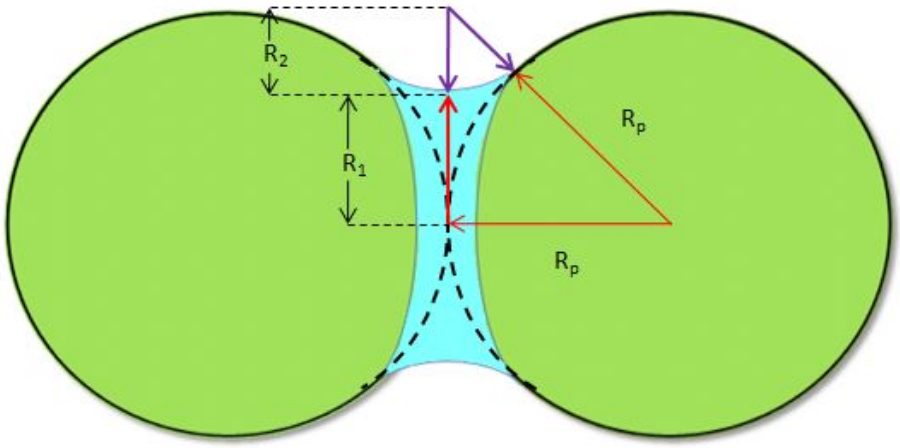

Fig. 27. Capillary condensation (light blue) between two spherical colloidal particles (green). R_1 and R_2 are the principal radii of curvature of the meniscus, and by convention, R_1 is negative and R_2 is positive. R_p is the radius of the colloidal particle.

Kelvin equation is obeyed by cyclohexane menisci with a mean radius of curvature (R_m, see next paragraph) as low as 4 nm. Interestingly, the value for surface tension of cyclohexane calculated from their experiments ($\gamma = 25.5\, mJ/m^2$) agrees well with γ obtained by conventional methods.

For a "neck" of liquid between two supports, the radius of curvature is characterized by a paraboloid of revolution [42]. Figure 27 shows a typical meniscus between two colloidal particles. A pressure difference exists across both the solid-liquid (S-L) and the liquid-vapor (L-V) interfaces, due to interfacial curvature. The mean radius R_m is represented by $1/R_m$=$1/R_1$+$1/R_2$.

Capillary condensation occurs when width of a pore, for example between silica particles in a hexagonal close-packed array, is a few times greater than the adsor-

bant molecule diameter and that the temperature is below the pore critical temperature. The critical point of the substance is lower in these voids because the confined molecules experience a reduction in number of nearest-neighbor molecules which results in a shift of the phase coexistence curve. When an ambient vapor condenses in this interparticle void, the condensate liquid has a highly curved liquid-vapor (L-V) interface due to the extremely small sizes of the neighboring nanoparticles. This results in a pressure difference across this interface, which in turn favors condensation of the material according to equation (4.6) [43], which is form is a modified version of the Kelvin equation (4.5). Figure 27 shows what is referred to as R_1 and R_2 in equation (4.6):

$$RTln(\frac{P_o^{Capillary}}{P_o}) = \gamma^{L-V} V_m (\frac{1}{R_1} - \frac{1}{R_2}) \tag{4.6}$$

where

R	= Universal gas constant
T	= Temperature
P_o	= Standard vapor pressure
$P_o^{Capillary}$	= Vapor pressure due to capillary condensation
V_m	= Molar volume of the liquid condensate
γ^{L-V}	= Surface tension at the liquid-vapor interface
R_1, R_2	= Radii characterizing the liquid-vapor (L-V) interface in figure 27

Capillary condensation is a purely physical process, where hydrophobic, hydrophilic, reactive and inert molecules can all be easily condensed, but they do have to have a reasonably high vapor pressure. The variables temperature T and pressure P represent the need for thermodynamic stability of the system, which is provided by the radius of curvature of the particles on the right of equation (4.6). From equation

(4.6), it is easy to see there is an inverse relationship between the amount of observed capillary condensation and radius of curvature of the particles, and the amount of capillary condensation is thus particle size-dependent; larger particles in a hexagonally close-packed array get progressively less capillary condensation.

B. Procedure

In this work, we are interested in using capillary condensation as a synthesis method for patchy particles. Capillary condensation in 2- and 3-D close-packed structures has been reported before. Yan *et al.* [44] have used a face-centered cubic (fcc) array of silica particles as a template to produce disk-like polystyrene pieces via capillary condensation. Gemici *et al.* [41] have capillary-condensed hydrophobic and hydrophilic reagents into layer-by-layer assemblies of poly(allylamine hydrochloride) and various sizes of silica particles to impart anti-reflection properties to their films. They also used poly(dimethyl siloxane) capillary condensation as a way to avoid adventitious water condensation, a common problem in assembled nano-arrays in humid conditions. However, capillary condensation has not yet been used as a method to fabricate patchy particles. Silica particles of various sizes with gold patches have been produced, as described below. Further experimental details of the experimental procedure and sample preparation for analysis via FTIR, SEM, OM and zeta potential measurements can be found in Chapter V.

1. Silica Particle Synthesis

Silica particles were synthesized using the direct and regrowth methods. Stöber [45] pioneered the direct synthesis method in 1968, while Giesche [46,47] built on it further to offer more monodisperse silica particles. Briefly, both methods involve the hydroly-

sis of tetraethylorthosilicate (TEOS) to produce silica with ethanol as by-product, the difference being whether the reagents are mixed quickly and directly (direct method) or added continuously at a particular rate (regrowth method).

2. Evaporative Self-Assembly

Once synthesized, silica particles are assembled into close-packed structures using evaporative self-assembly [48]. In essence, when a clean substrate is vertically placed in a colloidal silica particle dispersion and as the solvent (in this case, ethanol) evaporates, the particles are drawn to the meniscus, where they form a high quality fcc crystal. By knowing the volume fraction of the silica spheres in a given dispersion, it is possible to calculate the number of monolayers of hexagonally close-packed silica that will form on the substrate [48]. The goal in this research work is to create a closed-packed monolayer of silica spheres on a silicon wafer substrate (cleaned in piranha solution), however, in practice it is not easy to achieve. The number of layers tends to vary throughout the substrate, likely due to vibrations and thermal gradients in the oven and the higher polydispersity of larger silica particles which causes defects in the fcc crystals.

3. Capillary Condensation

The monolayer of silica spheres on the silicon substrate is now put into a special setup to perform capillary condensation, as shown on page 73 in Chapter V. The capillary condensation results in small patches of capillary-condensed substance throughout the close-packed array, represented in a schematic in Figure 28, according to equation 4.6. The silicon wafer with close-packed silica spheres is placed inside a large weighing bottle with ground glass, along with a smaller 20 mL vial that contains a 2 mL glass vial with the substance to be condensed. In this work, two substances have been

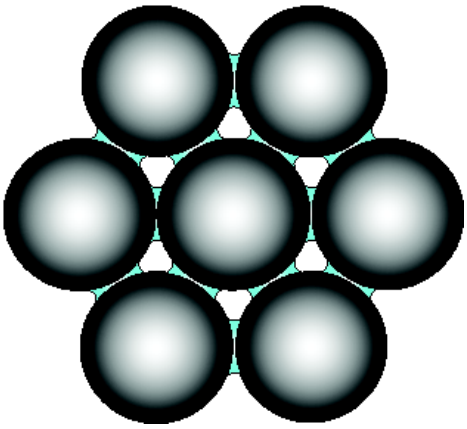

Fig. 28. Bridges of liquid condensate between close-packed silica particles in a colloidal crystal.

condensed to create patches on the silica particles:

- 3-aminopropyltriethoxysilane (APTES)
- 3-mercaptopropyltrimethoxysilane (MPES)

While capillary condensation itself is a therymodynamically-driven phenomenon, both APTES and MPES are reactive towards hydroxyl groups on the colloidal silica surface, and once APTES or MPES are physically condensed in the voids of the hexagonal silica particle array, they covalently bond to the silica particle surface. The reaction mechanism is similar to that of tetraethylorthosilicate hydrolysis, as described in detail in Chapter V, and the resultant structure can be seen in Figure 29 for APTES and in Figure 30 for MPES. Methanol (for MPES) and ethanol (for APTES) vapor is produced as a by-product of the reaction.

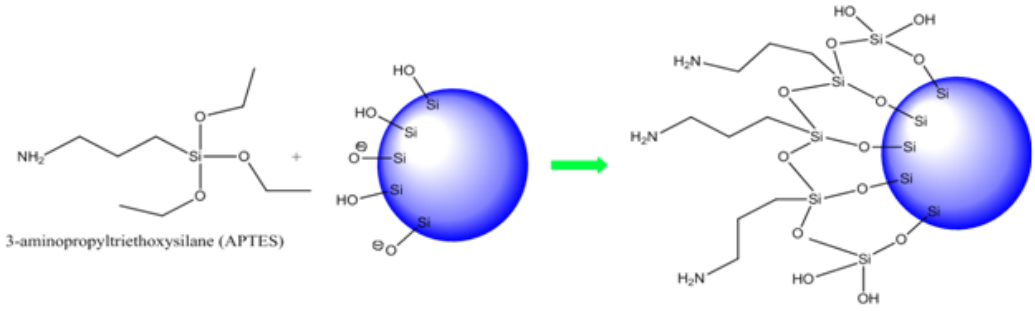

Fig. 29. Reaction schematic for APTES covalently bonding to silica particle surface after capillary condensation.

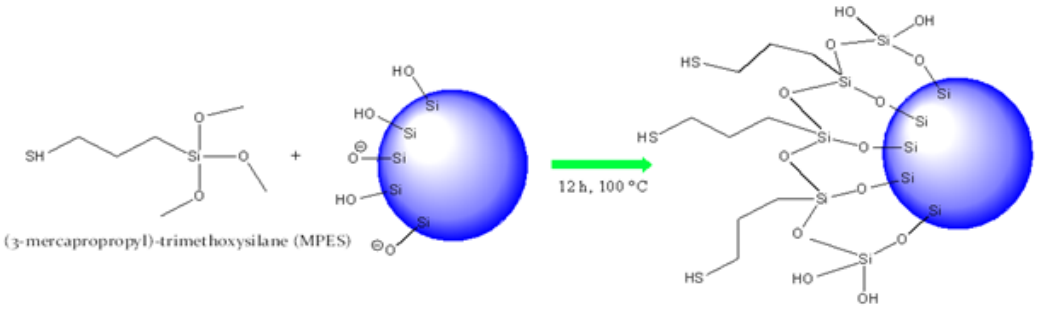

Fig. 30. Reaction schematic for MPES covalently bonding to silica particle surface after capillary condensation.

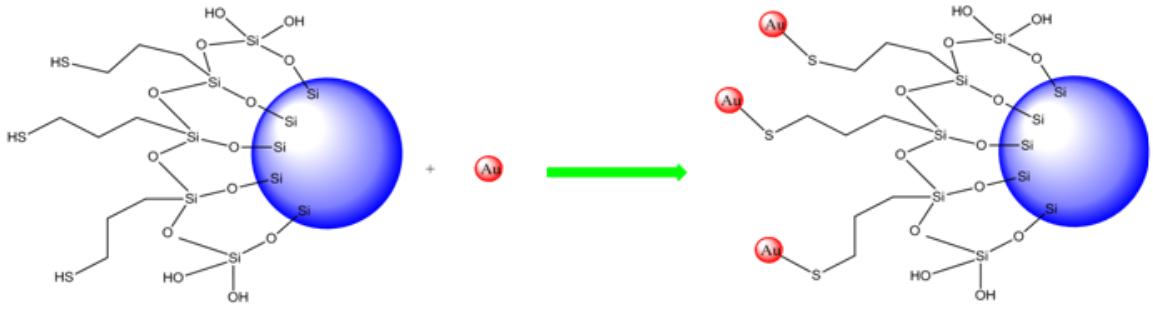

Fig. 31. Schematic of gold nanoparticles bonding to the thiol group on MPES-coated silica particle.

4. MPES: Reaction with Gold Nanoparticles

Once the silica particles are covered in capillary-condensed MPES patches, the particles are functioanlized with gold nanoparticles of 14 nm in diameter. Since the thiol group on the MPES molecule has high affinity for gold, theoretically the nanoparticles should only bind at the sites where capillary condensation is present. Figure 31 shows the particle structure once it has been coated with gold nanoparticles.

5. APTES: Patch Characterization via Zeta Potential

Once the silica particles are covered in capillary-condensed APTES patches, the zeta potential of the particles is measured. The values obtained are compared with a silica particle fully functionalized with APTES, as well as the as-synthesized silica particle with no APTES. More details are discussed in the next section.

C. Sample Characterization

1. Scanning Electron Microscopy (SEM)

a. Gold Nanoparticle Functionalization

SEM images of several patchy particles are shown in Figure 32. It is possible to see how the size of the condensation on the particles varies with particle size, and is reflected in the changing size of the gold nanoparticle patches. As particles decrease in size below 100 nm, capillary condensation can be used to create a full coating instead of discrete patches. In parts A and B of Figure 32, 150 nm and 490 nm diameter silica particles can be seen with gold nanoparticles bonded to the thiol condensate patches. The nanoparticle functionalization does not have 100% yield, for a number of reasons. However, we believe that the condensation process has a much higher success rate than the later attachment of nanoparticles. As can be seen in Figure 32 A, the particles are not always regularly packed, due to polydispersity or other defects that occur during crystallization. Another contributing factor is the process itself; attaching the gold nanoparticles to the silica spheres is a heterogeneous reaction with a number of washing steps, after which chunks of the crystal are removed from the substrate by sonication for SEM imaging. The SEM images do show that the gold nanoparticles attach to areas between the particles, presumably where the thiol groups are present. Also, Figure 32 C clearly shows an individual particle with three patches at 120° with respect to each other, as a result of the close-packed crystal structure. This, and further characterization outlined below, lead us to believe that the procedure does work as intended.

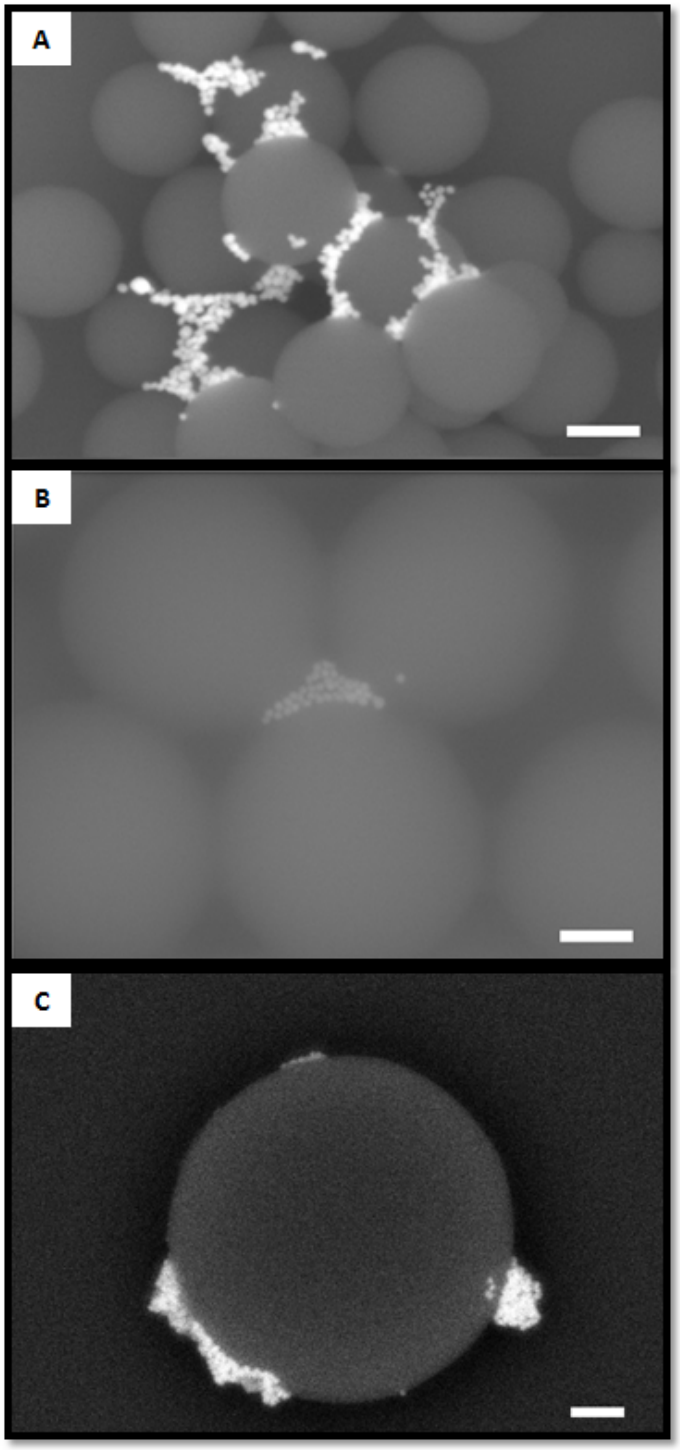

Fig. 32. Capillary condensation in a group of particles (A,B), and an individual particle with gold nanoparticle "patches" (C): A - 150 nm silica, B - 490 nm silica spheres, C - 455 nm silica with 3 gold nanoparticle patches 120° apart. Scale bar = 100 nm.

b. Gold Nanoparticle Formation In-Situ

In the hopes of improving patchy particle yield, gold nanoparticles have been synthesized in situ. A typical synthesis involves a close-packed array of silica particles (16 nm, 430 nm and 710 nm were attempted) on a glass slide or silicon wafer, where MPES was capillary-condensed for 12 hours. 5 mL of 0.1 mM $HAuCl_4$ was added to each sample and allowed to react for 1 hr. Samples were then rinsed with copious amounts of water and ethanol, then allowed to dry. Next, samples were reacted with 10 mM $NaBH_4$ for 1 hr. Finally, particles on glass slide were sonicated and deposited on silicon wafer pieces, allowed to dry and analyzed via SEM. Samples with silicon wafer as substrate were rinsed and taken to SEM directly. A sample SEM image, BSE mode, is shown in Figure 33. Here, 430 nm silica particles are shown, with the resultant patchy particles on silicon wafer substrate (no sonication). These particles proved too fragile for sonication, and as the SEM image indicated even without sonication the patches formed are not of good quality.

2. Energy-Dispersive X-ray Spectroscopy (EDX)

EDX spectra were obtained of various silica particle assemblies to confirm prescence or absence of capillary-condensed MPES. Relevant SEM and EDX spectra are shown in Figure 34. In this figure, SEM images and EDX spectra of close-packed assemblies of silica particles, diameter 98 nm (A-D) and 430 nm (E-F) are shown. The SEM images are located on the left, with corresponding EDX spectra on the right. Relevant characteristic x-ray energies are listed in Table I.

SEM images in part A and C represent different locations on the same sample; part A shows close-packed silica assembly, while part C shows an area of the silicon wafer with scattered silica spheres (likely the end of the subtrate that was immersed

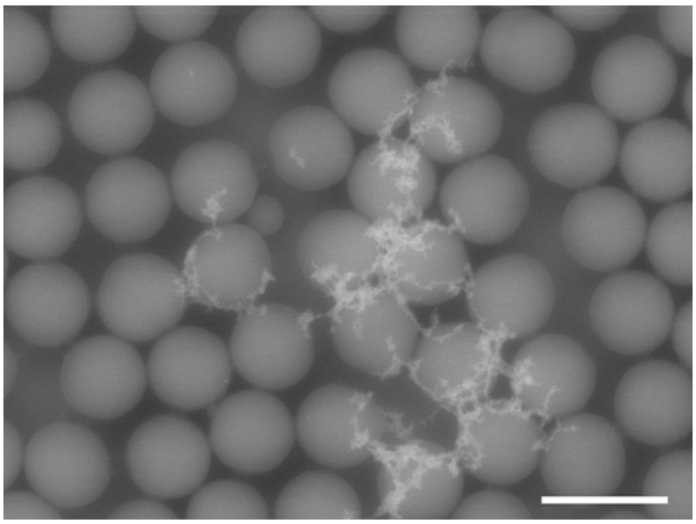

Fig. 33. SEM image, BSE mode, of 430 nm ordered silica particles after capillary–condensation of MPES and in-situ Au nanoparticle formation. Scale bar = 1 μm.

into the silica dispersion during evaporative self-assembly, but below the ethanol meniscus, where crystallization typically occurs as the ethanol evaporates). As the EDX spectra indicate, sulfur x-ray peak at 2.307 keV in part B is present in the close-packed array of silica spheres, while noticeably absent in part D, which refers to the SEM image in part C, with a few scattered silica spheres. The absence of MPES is expected since for capillary condensation to occur, the spheres need to be touching in a regular array to create nano-pores. Adventitious macroscopic condensation (occurs if sample is improperly removed from oven after capillary condensation is finished, see Chapter V) is also successfully avoided, which otherwise would indicate sulfur presence with or without close-packed colloidal silica particle presence. The signals of oxygen at 0.525 keV and carbon at 0.277 keV have also dimished in part D, which is expected since there is no MPES (source of C and S peaks) and almost no silica (O peak), and the silicon signal intensity at 1.739 keV has increased dramatically relative to part B as the detector is primarily picking up x-rays from the silicon wafer substrate. SEM images of 430 nm particles in part E also show successful MPES capillary condensation with a sulfur x-ray peak at 2.307 keV in part F. Other silica particle sizes forming fcc arrays showed similar behavior of MPES capillary condensation.

Unfortunately, while gold nanoparticles attached to MPES-condensed silica particle arrays could be easily visualized in SEM, the signal produced was too weak to be detected in EDX. Similarly, mapping on silica particle arrays to visualize more precisely the location of MPES condensate in relation to the silica particles failed due to inability of detector to focus on x-ray emission into such small sample areas.

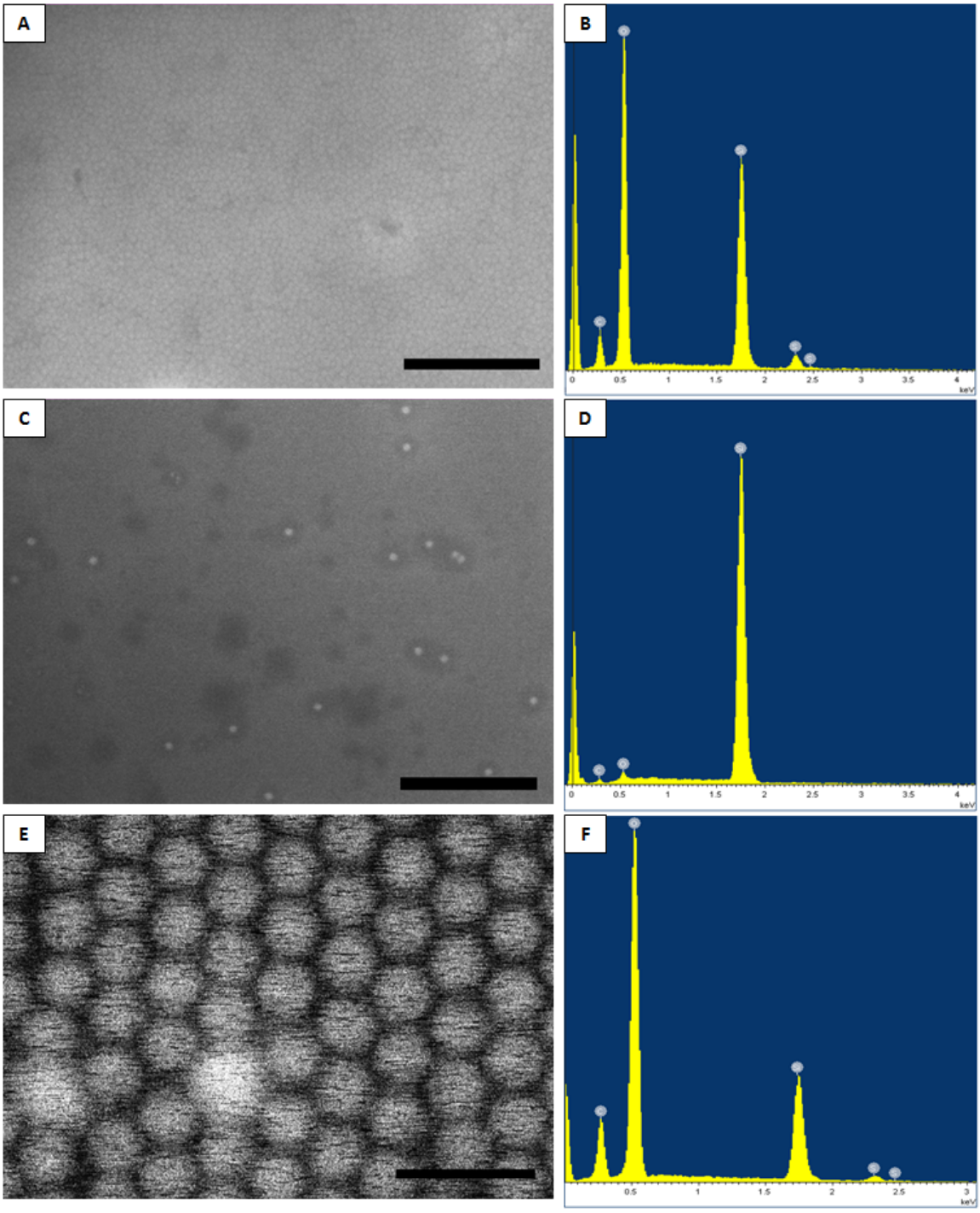

Fig. 34. SEM (A,C,E) and EDX (B,D,F) spectra of 98 nm silica particles (A-D) and 430 nm silica particles (E-F) with capillary-condensed MPES. Scale bar = 2 μm.

Table I. Characteristic x-rays of several elements

Element	Electron Transmission Type	Characteristic X-ray (keV)
Carbon	Kα	0.277
Oxygen	Kα	0.525
Silicon	Kα	1.739
Sulfur	Kα	2.307
Gold	M	2.120

3. Fourier Transform Infrared Spectroscopy (FTIR)

Fourier Transform Infrared Spectroscopy (FTIR) has been used to confirm capillary condensation of MPES into a close-packed array of silica spheres. Figure 35 shows three FTIR spectra, namely that of pure MPES, 410 nm close-packed silica spheres on a silicon substrate, and MPES capillary-condensed (C.C. MPES) into the voids of a close-packed silica sphere array on a silicon wafer subtrate. For sample preparation, please see Chapter V. Sulfur and carbon are two elements that are not present in silica particles, and thus the absorbances of these functional groups can be used to prove prescence of MPES on the fcc silica array after capillary condensation. With the consultation of infrared spectroscopy tables [49, 50], as well as several pertinent journal articles [51–53], the relevant infrared absorption frequencies have been compiled in Table II. In Table II, s, m and w refer to strong, medium and weak absorbances, respectively.

The wavenumbers (cm^{-1}) of numerous peaks in Figure 35 have been labelled, and the color of each corresponds to the spectrum of the same color. Starting with

Table II. Absorption frequencies of various chemical groups

Chemical Group	Band, cm^{-1}
-S-H	2600-2450 (w)
-S-CH_2	2950-2940 (m) 2880-2845 (m) 1440-1415 (m) 1270-1220 (s)
-Si-O-	1100-1000
-Si-OH	870-820
-Si-C-	690-850
-OH	3400-3700, very broad
-CH_2-	1420-1480 715-760
-O-CH_3	1430-1470

the spectrum of pure MPES (blue curve), there are several noteworthy peaks. 2840 cm^{-1}, 2945 cm^{-1} and 1472 cm^{-1} correspond to -S-CH_2 stretches, while 2564 cm^{-1} corresponds to the -S-H stretch. These peaks are, as expected, absent from the FTIR spectrum of close-packed silica spheres (red curve). The peak at 1472 cm^{-1} could correspond to -O-CH_3 stretch (generally found in 1430-1470 cm^{-1} range), but this same region also shows absorption of -CH_2- (1420-1480 cm^{-1}). The generally strong Si-O peak at 1089 cm^{-1} (MPES) and 1104 cm^{-1} (silica) is present in both curves since both materials posess this chemical group. The peaks below 1000 cm^{-1} for MPES are generally hard to classify as they correspond to an overlap of methylene groups (715-760 cm^{-1}), Si-C (690-850 cm^{-1}) and Si-O assymetric stretch (795 cm^{-1}). In the case of silica, the broad peak at 3444 cm^{-1} is characteristic of the -OH groups, which are present in abundance on colloidal silica synthesized using the Stöber and Giesche methods. This peak is absent in the pure MPES spectrum. Si-OH assymetric vibration for colloidal silica is roughly at 965 cm^{-1} [53], but the region below 1000 cm^{-1} is considered a superimposition of various SiO_2 peaks and SiOH absorption bands [53].

The close-packed silica array with capillary-condensed MPES (green curve) shows clear indications of MPES presence. The -S-CH_2 bands are still present, though quite small (2840 cm^{-1}, 2941 cm^{-1}) as well as the peak at 1466 cm^{-1}. This is easier to see in Figure 36, where the orange curve represents the difference between the red and green curves from Figure 35, which is the capillary-condensed MPES only. The peak corresponding to ether and methylene functionalities at 1472 cm^{-1} is still present, which means it is more likely the methylene band as all of the -O-CH_3 groups should have hydrolysed, once capillary condensed in the silica particle array, as they are quite reactive. The vibration of -S-H at 2564 cm^{-1} is no longer visible, but that is not surprising since the peak had small absorption intensity even in the blue curve

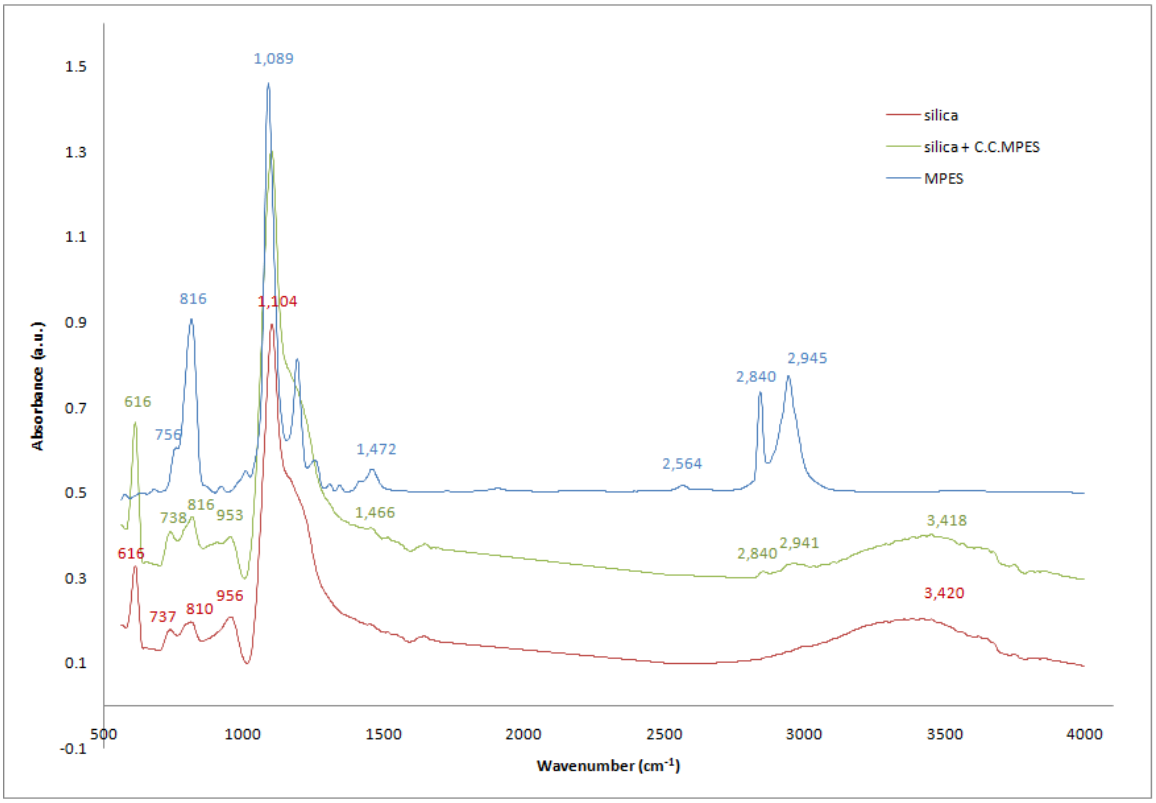

Fig. 35. FTIR spectra of pure MPES (blue), 410 *nm* close-packed silica on silicon wafer (red) and 410 *nm* close-packed silica on silicon wafer after capillary condensation of MPES (green).

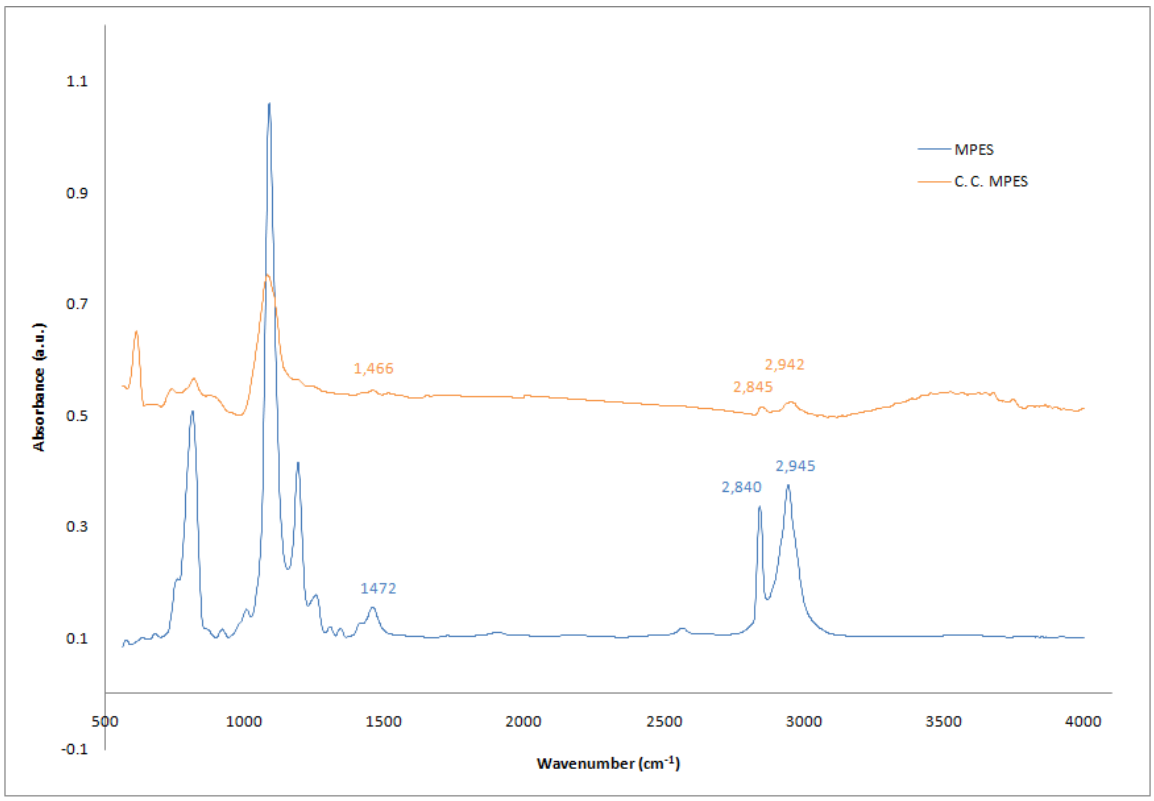

Fig. 36. FTIR spectra of pure MPES (blue) and capillary-condensed MPES only (orange), with close-packed silica subtracted.

(pure MPES). It is very difficult to detect such minute amount of MPES as through capillary condensation, and while most of the orange curve in Figure 36 corresponds to peaks found in the spectrum of close-packed silica, the few sulfur peaks are still visible, and I believe this is good indication of successful capillary condensation as measured by FTIR.

4. Optical Microscopy (OM)

Due to the sub-micron size of the patchy particles, optical microscopy was not employed much since it is incapable of the resolution necessary for sample analysis. It was, however, used to image evaporative self-assembly of silica particles, with an example image in Figure 37.

Part A shows the well-ordered structures that can be produced, while part B shows the importance of avoiding any impurities or highly polydisperse samples, as the number of layers of silica particles will fluctuate. It should be noted that in part A there are plenty of defects in the structure, such as kinks, which are difficult to eliminate entirely due to thermal gradients in the oven, small vibrations, etc.

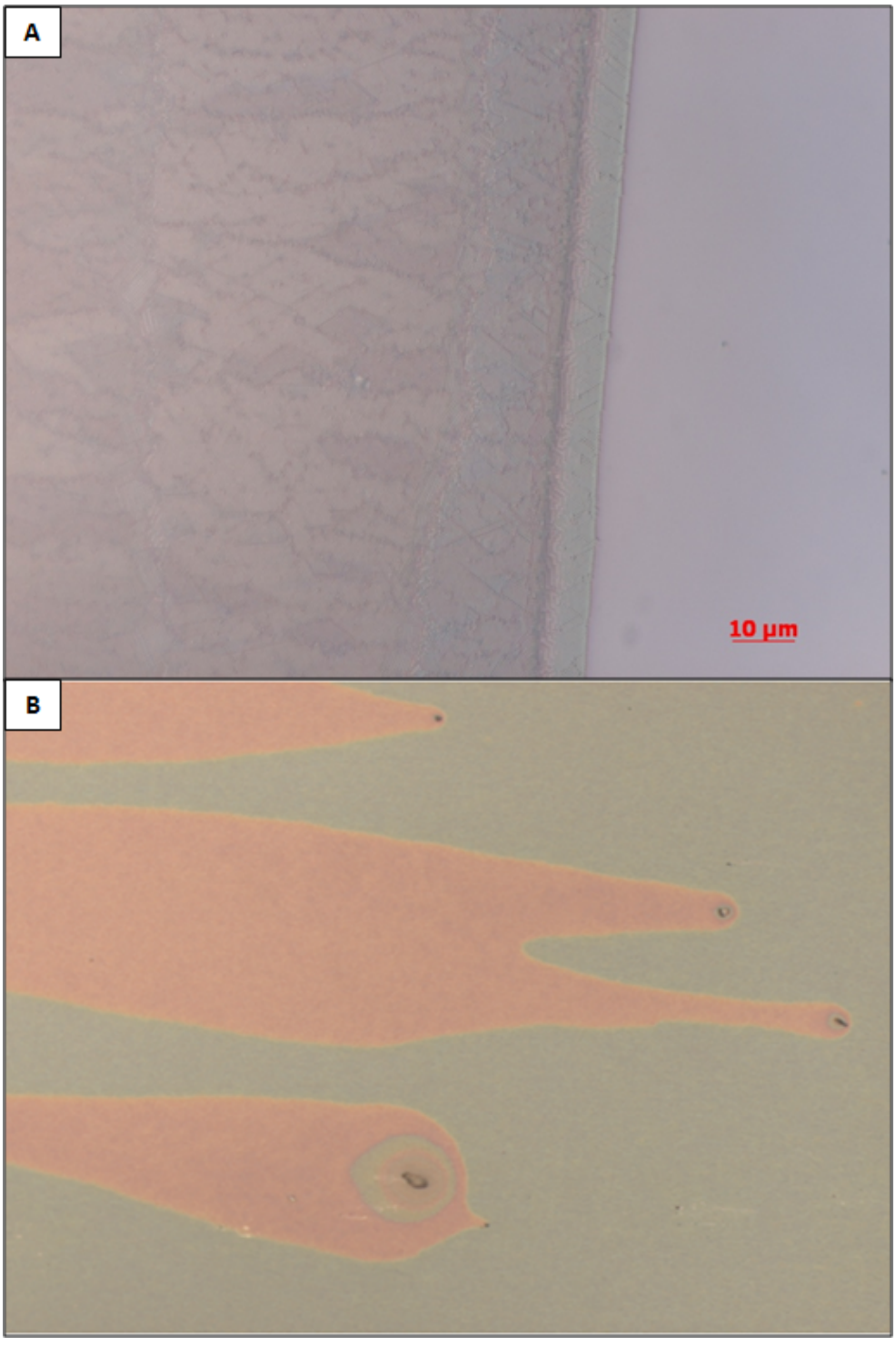

Fig. 37. Optical microscope image of evaporative self-assembly of silica particles: A - 490 nm, B - 150 nm.

Table III. Zeta potential values for silica spheres as synthesized, completely silanized with APTES, and functionalized through capillary condensation

Sample	Zeta Potential (mV)
800 nm, as synthesized	-31.62
800 nm, APTES functionalized	46.57
800 nm, capillary condensation	-21.98
490 nm, as synthesized	-34.34
490 nm, APTES functionalized	68.37
490 nm, capillary condensation	35.07
150 nm, as synthesized	-18.89
150 nm, APTES functionalized	45.87
150 nm, capillary condensation	29.44

5. Zeta Potential

The zeta potential of various silica particles with capillary-condensed APTES is compared with silica particles fully functionalized with APTES, as well as the as-synthesized silica particles with no APTES. The pH of the solutions is adjusted to 5, which based on the pKa of the amine group (9-10), should render the amine groups positively charged, and is above the isoelectric point of silica. Thus the zeta potential of silica particles functionalized with APTES should be very positive, while the zeta potential of as-synthesized particles is strongly negative due to the abundance of hydroxyl groups as a result of the Stöber/Giesche synthesis methods. Hence, the expected value of capillary-condensed APTES silica particles should be something

inbetween, and that is what has been observed in the obtained zeta potential data listed in Table III. From this it can be seen that the spheres have been modified during the capillary condensation process, and that they are only partially functionalized by the silane. This modification of zeta potential due to capillary condensation is least for the 800 nm spheres, which would be expected to have the smallest patches of condensate based on equation (4.6).

D. Discussion

The synthetic route for novel patchy particles has been described with multiple characterization techniques used to verify the success of the synthetic method. SEM images show gold patches on particles of various sizes, and a general decrease in patch size is observed with increasing silica particle size. EDX and FTIR spectra confirm the success of MPES capillary condensation, and the absence of adventitious macro-condensation. Zeta potential measurements of APTES-functionalized particles confirm capillary condensation since the particles show intermediate, slightly negative zeta potential to that of a fully APTES-functionalized silica particle, and the as-synthesized silica particle.

Unfortunately, the nanoparticle functionalization does not have 100% yield. Some of the possible causes include polydispersity of the silica spheres. The Giesche method is difficult to use for making larger particles, and thus the Stöber silica spheres have been used, albeit with higher polydispersity. Thermal gradients in the oven, vibrations and any imperfections on the substrate also hinder the formation of a perfect fcc silica crystal necessary for successful capillary condensation. Attaching the gold nanoparticles itself includes numerous wash steps, and the patchy particles are generally fragile to excessive mechanical aggitation or prolonged sonication.

In terms of applications, these patchy particles could serve as a potential platform for surface-enhanced Raman spectroscopy (SERS) [54]. This technique takes into account the fact that Raman scattering is enhanced when molecules are adsorbed onto a metal surface. Unlike other methods, Raman spectroscopy is capable of providing highly resolved vibrational information about the molecule of interest and does not suffer from rapid photobleaching [54]. This technique requires a noble metal nanostructure in close proximity to each other but without huge clumps, which would allow one to control it.

E. Future Work

There is still potential for further experiments to improve this new synthesis route. Possibilities to improve particle yield includes using smaller gold nanoparticles that will be less sterically hindered and will therefore form better coverage of the MPES-condensed patches. Improving synthetic methods for silica particles will increase monodispersity and investing in a good quality vibration table could all help to improve the quality of the evaporative self-assembly of the silica spheres. Further experiments are still needed to quantize the relationship between silica particle size and the size of the resultant capillary-condensed APTES and MPES patch. Finally, other substances can be tested for capillary condensation, and the improved yield will allow testing self-assembly behavior and testing potential applications, such as surface-enhanced Raman spectroscopy.

CHAPTER V

EXPERIMENTAL SECTION

All reagents were used as received from supplier, without further purification. DI water refers to deionized water with resistivity of 18.2 $M\Omega \times cm$, obtained using Millipore Direct-Q 3 UV water purification system.

A. Substrate Preparation

Silicon wafer (Wafer World) was typically used, with glass slides (VWR) on occasion. Silicon wafer was cut into rectangular pieces using a diamond knife, typical dimensions are 1/2" x 1 1/2". The silicon wafer pieces were cleaned in piranha solution (H_2SO_4(EMD):H_2O_2(BDH, 30%) 3:1) for 1 hr, after which the pieces were rinsed thouroughly with DI water, sonicated in DI water for at least 1 hr and dried using N_2 gas filtered through a Norgren Excelon B73G filter.

B. Colloidal Silica Synthesis

Silica spheres were synthesized using the Stöber [45] and Giesche [46, 47] methods. These methods can also be classified as direct and regrowth syntheses, respectively.

1. Direct Method

Discovered by Stöber in 1968, various silicon alkoxides dispersed in an ethanol-water solution undergo ammonia-catalyzed hydrolysis to produce silica particles in the 50 nm - 2 μm range [45]. The net reaction can be seen in Figure 38 [55]. Reaction 1 represents the hydrolysis of tetraethylorthosilicate (TEOS) to form the monosilicic acid, a reactive intermediate, and an alcohol as a side-product. Reaction 2 involves

monosilicic acid undergoing condensation with itself (and also with hydroxyl groups on newly-formed silica particles) to form silica particles. Large particles grow at the expense of smaller particles due to Ostwald ripening, with final particle size determined by the ratio of TEOS, ammonia and water. Ammonium hydroxide (EMD) was used instead of ammonia in this work, as it is easier to work with than ammonia gas. However, one must take into account the amount of water added with ammonium hydroxide to maintain correct water concentration in the reaction. TEOS (Acros Organics, 98 %), DI water and NH_4OH (EMD) concentrations were achieved by addition of ethanol (EMD, anhydrous, denatured) which itself does not participate in the reaction. Various reactant ratios, with resultant silica particle diameter and standard deviation are outlined by Giesche [46], and are used in this work. Some pertinent SEM images of synthesized silica spheres can be seen in figure 39, with some synthesized in batches as large as 800 mL.

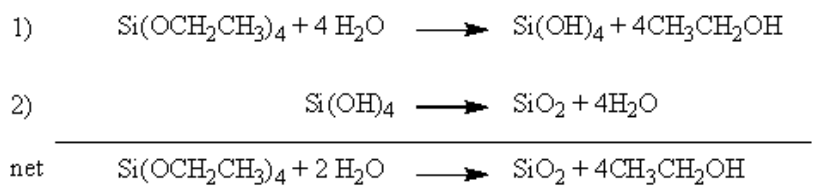

Fig. 38. Reaction steps for silica colloidal particle formation.

2. Regrowth Method

One of the main disadvantages of the Stöber method is the relatively high polydispersity of the resultant particles, especially at sizes less than 150 nm. The reason

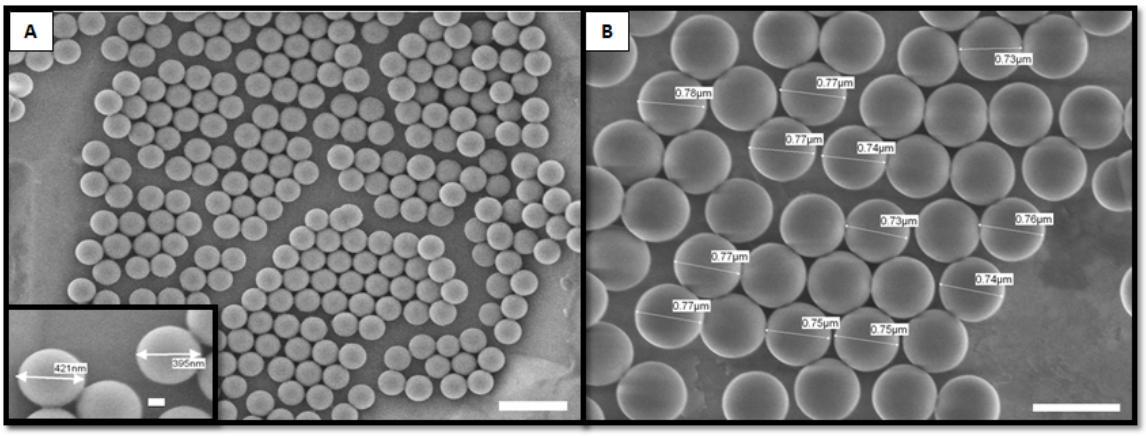

Fig. 39. SEM images of silica spheres synthesized using the direct method. A - 410 nm, scale bar = 1 μm, 100 nm (inset), B - 755 nm, scale bar = 1 μm.

for this is the difficulty of controlling the onset of particle nucleation. The Giesche method involves making very small silica particles, termed "seeds". This allows for the nucleation phase of the reaction to be controlled and separated from further reaction steps. The amino acid L-arginine (predominantly basic due to the guanidium group with pK_a=12.10) is used instead of ammonia to stabilize the silica spheres, and its chiral nature allows for more precise control of resultant silica sphere size. The reaction scheme is shown in Figure 40. A typical procedure, as developed by Hartlen *et al.* [5], involves heating 6.9 mL water (383 $mmol$), 9.1 mg (0.0522 $mmol$) L-arginine (EMD) and 0.45 mL (4.27 $mmol$) cyclohexane (Mallinckrodt Chemicals) to 60°C, with stirring slow enough as not to disturb the cyclohexane/water interface (it is possible to remove the cyclohexane altogether, but resulting spheres are slightly smaller and less monodisperse [5]). Then, 0.55 mL TEOS (2.46 $mmol$) is added, and reaction temperature and stirring maintained for 20 hours. Resultant silica particles

are typically $24nm \pm 3nm$, as can be seen in Figure 41.

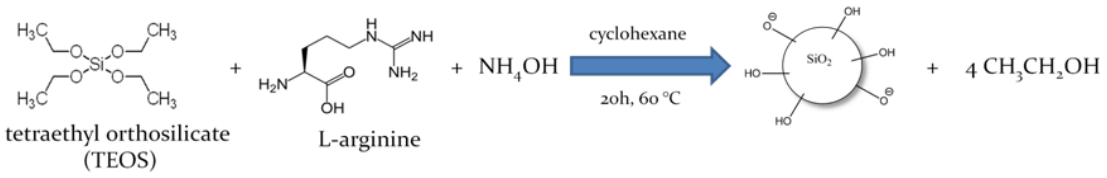

Fig. 40. Reaction scheme for silica seed formation.

The seeds can further be regrown to generate larger spheres using the regrowth method, as described by Giesche [47] and shown schematically in Figure 42. The process can be described by equations (5.1) and (5.2). Both TEOS and ammonia are added gradually, with TEOS addition rate predicted by equation (5.2). For better results, TEOS should be diluted with ethanol to TEOS:ethanol 1:3, by volume. Sample SEM images can be seen in Figures 43 and 44 for 98 nm and 150 nm silica particles, respecitively. Compared to Figure 39, the monodispersity of spheres is markedly higher, as evidenced by very nice closely-packed hexagonal arrays of particles.

$$\frac{M_{TEOS(added)}}{M_{TEOS(original)}} = \left(\frac{D_{final}}{D_{initial}}\right)^3 - 1 \tag{5.1}$$

where

$M_{TEOS(added)}$ = Mass of TEOS added during reaction

$M_{TEOS(original)}$ = Mass of TEOS present originally

$D_{initial}$ = Diameter of seed silica particle

D_{final} = Diameter of regrown silica particle

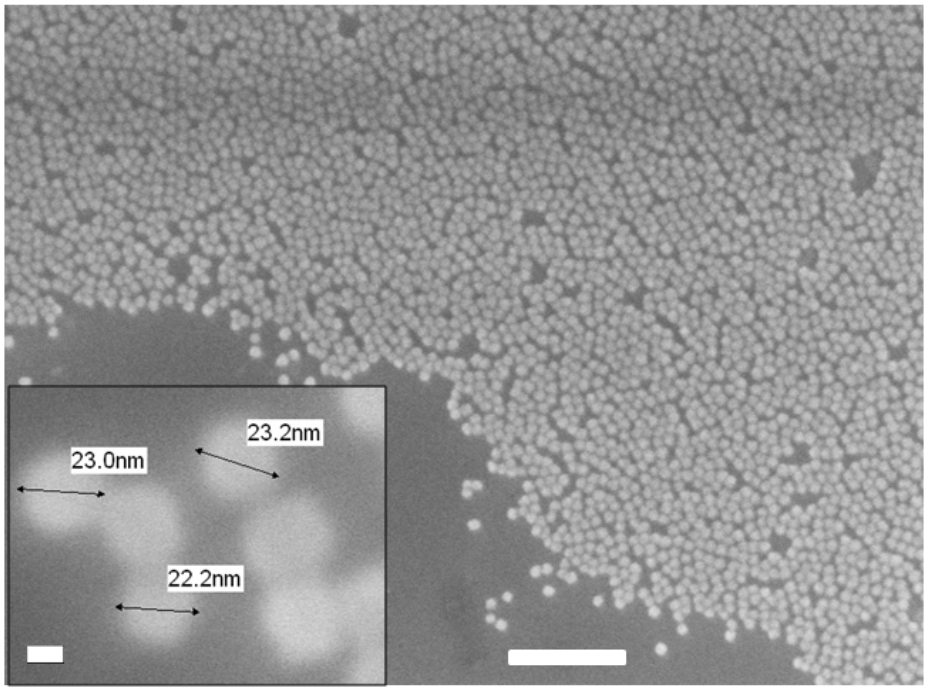

Fig. 41. SEM image of silica seeds, scale bar = 200 nm. Inset shows a close-up of the same image, scale bar = 10 nm.

$$t = 5\frac{log\left[\frac{M_{TEOS(added)}}{M_{TEOS(original)}}\right]}{log2} \tag{5.2}$$

where

$M_{TEOS(added)}$	= Mass of TEOS added during reaction
$M_{TEOS(original)}$	= Mass of TEOS present originally
t	= TEOS addition time (hour)

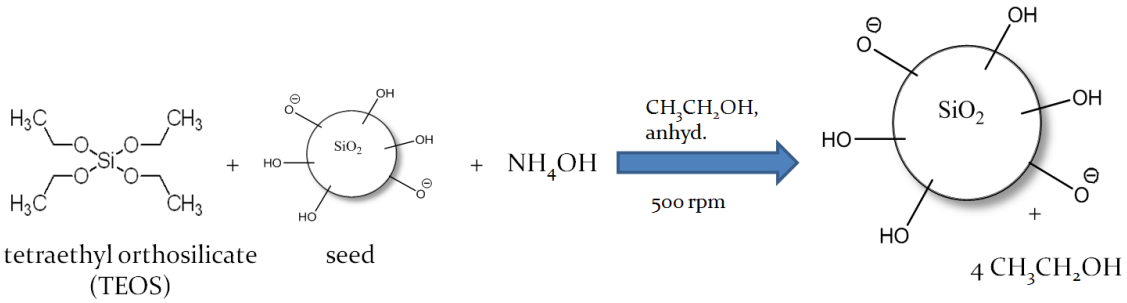

Fig. 42. Reaction scheme for silica seed regrowth via the Giesche method.

3. Characterization

Silica particles were characterized using SEM, with particle size of a given batch taken as an average of at least 30 particles. Once synthesized, all particles were redispersed in ethanol at least 3 times to remove any ammonium hydroxide and unreacted TEOS. The volume fraction of silica dispersion was determined by putting 5 mL of a given solution in a clean glass vial of known weight, and re-weighing the vial upon evaporation of solvent. The density of colloidal silica was assumed to be 2.2 g/cm^3 [55].

C. Evaporative Self-Assembly

A dispersion of colloidal particles can be crystallized onto a vertical substrate into a regular 2- and 3-dimensional array due to controlled evaporation of the dispersion solvent. The meniscus formed at the contact of the solution and substrate causes constant influx of solution as the solvent evaporates. Interparticle capillary forces between particles result in the continuous formation of close-packed structure during

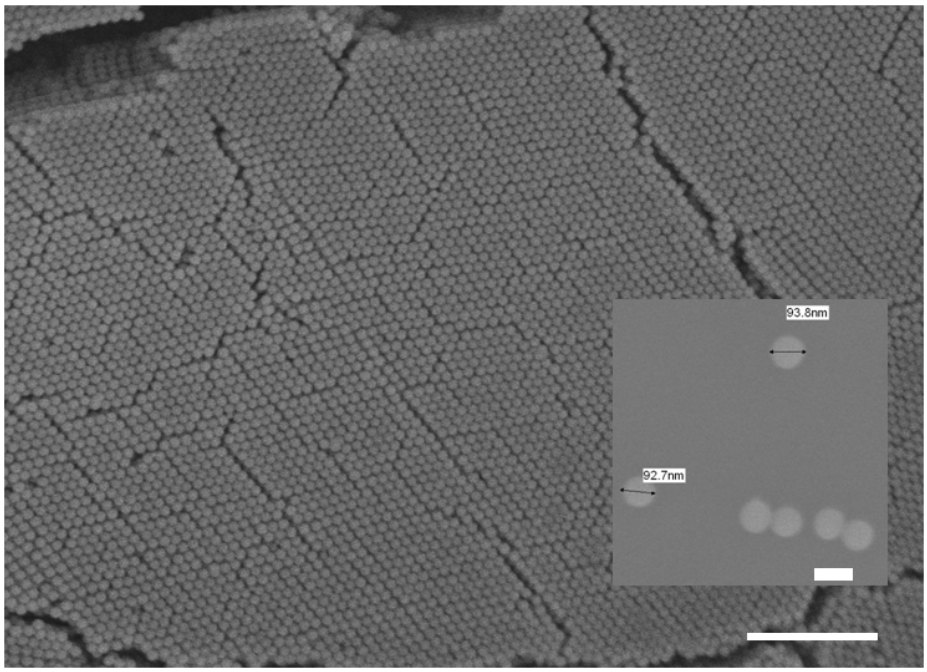

Fig. 43. 98 nm silica particles synthesized using the regrowth method. Scale bar = 1 μm, 100 nm (inset).

solvent evaporation. The number of close-packed layers can be described by equation (5.3) [48]. Film thickness is independent of evaporation rate [48], and this method has been successfully used for various colloidal particles. In this experiment, silica particles were used. All evaporations were done in ethanol (meniscus height = 310 μm [48]), and a typical setup can be seen in Figure 45, part A. Here a piranha-cleaned silicon wafer is placed inside a 20 mL vial filled with silica particles dispersed in ethanol at a known volume fraction. The vial is placed into an oven at $40°C$, being careful to minimize air fluctuations, temperature gradients and physical vibrations during evaporative self-assembly. Figure 45, part B shows a cross-section SEM image

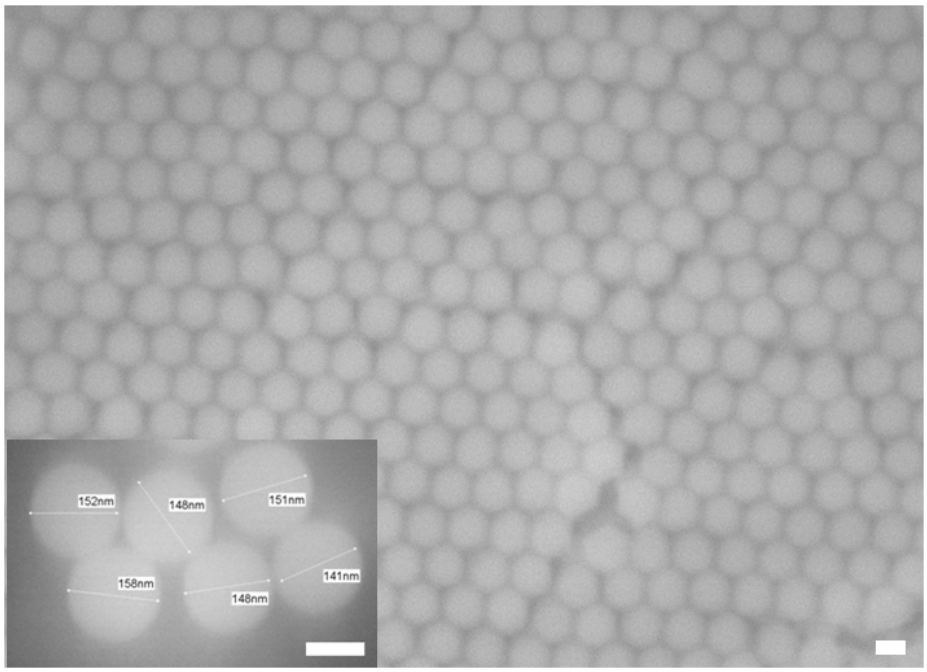

Fig. 44. 150 nm silica particles synthesized using the regrowth method. Scale bar = 100 nm.

of a monolayer of 410 nm silica spheres on a silicon wafer, while part C shows 3 layers of 200 nm particles. Unfortunately, the sedimentation velocity of particles larger than approximately 500 nm is larger than ethanol evaporation rate, and thus close-packed assemblies of inferior quality result without the application of lower pressure to increase the ethanol evaporation rate.

$$k = \frac{L\phi}{0.605d(1-\phi)} \tag{5.3}$$

where

k = Number of sphere layers

L = Meniscus height

ϕ = Particle volume fraction

d = Sphere diameter

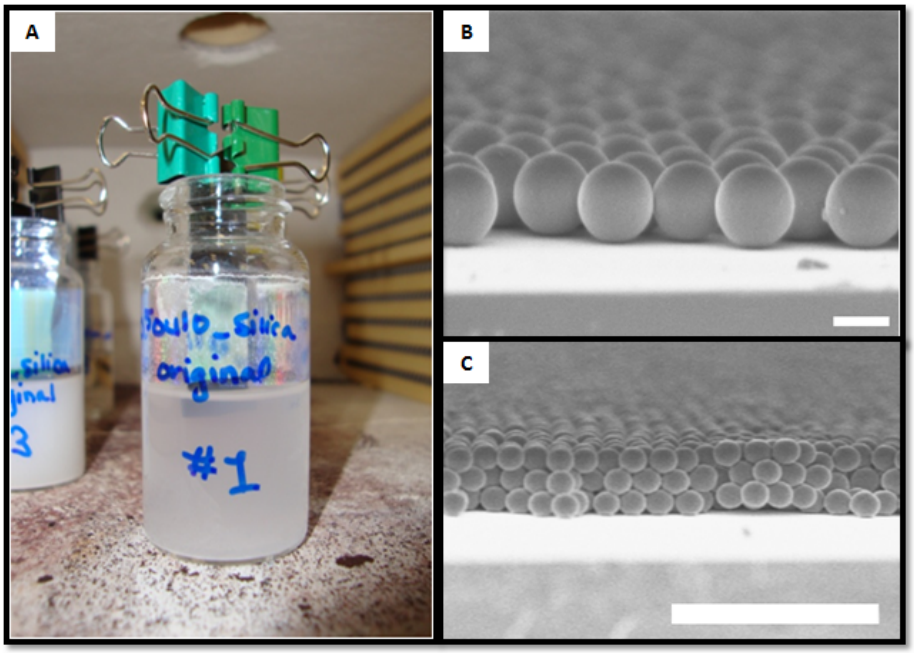

Fig. 45. A - evaporative self-assembly setup with silica spheres assembled on silicon wafer from an ethanol dispersion, B,C - SEM images of cross-section of silica layers on piece of silicon wafer formed via evaporative self-assembly; B - 410 nm, monolayer, scale bar = 300 nm, C - 200 nm, 3 layers, scale bar = 5 μm.

D. Gold Nanoparticle Synthesis

Gold nanoparticles were synthesized according to the literature [56], and the reaction scheme is shown in Figure 46. Typically, 50 mL of 1 mM $HAuCl_4$ (Alfa Aesar, 45% minimum Au content) in water was put into a round-bottom flask with a condenser and brought to a boil while stirring. The addition of 5 mL of 38.8 mM sodium citrate (BDH, disodium trihydrate) in water produced a color change from pale yellow to burgundy. After 10 minutes of reflux, the flask was removed from heat and was left stirring for an additional 15 minutes. Finally, the solution was filtered through a 0.45 μm nylon syringe filter to remove any large agglomerates. Particles produced were 14 ± 2 nm from SEM images, as shown in Figure 47 (the size of 30 plus particles was averaged to obtain this value).

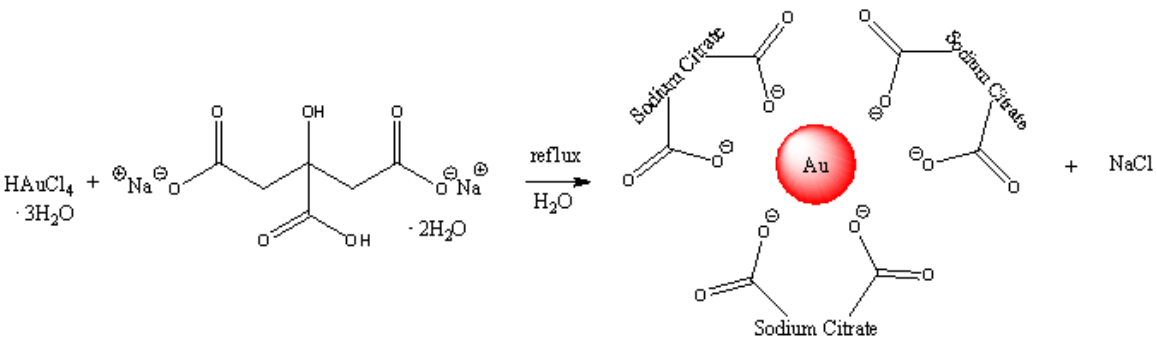

Fig. 46. Reaction scheme for gold nanoparticle formation.

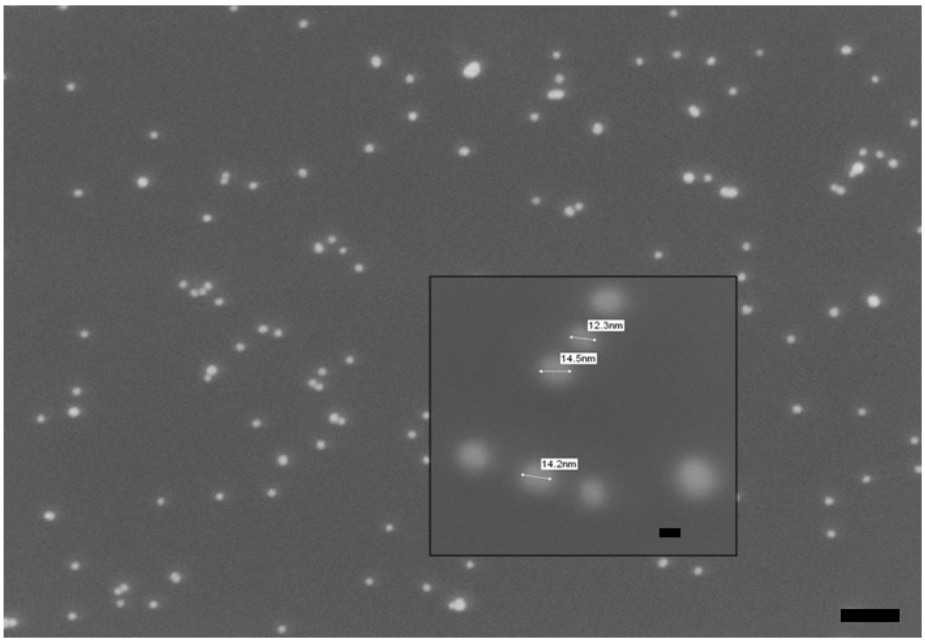

Fig. 47. SEM image of gold nanoparticles. Scale bar = 10 nm (inset) and 100 nm (main image).

E. Capillary Condensation

The setup for capillary condensation is shown in Figure 48. Typically, the substance to be condensed is placed inside a small 2 mL glass vial (orange for clarity in the figure), about 3/4 full. A secondary 20 mL glass container is used for mechanical stability and as a barrier between the substrate and condensate container. Finally, the 20 mL glass container is placed inside a large weighing bottle along with the substrate with close-packed silica on the surface obtained via evaporative self-assembly. The weighing bottle has ground glass on the cap for a tight seal. APTES (Aldrich) and MPES (Aldrich) both have a boiling point of 217°C and are reasonably volatile. After

testing several temperatures and condensation times, the experiment worked best at $100°C$ for 12 hours. Higher temperatures and longer condensation times tended to produce macroscopic condensation on the inner weighing bottle surface and the substrate, which is undesirable. It is also important to properly remove the substrate from the weighing bottle once the capillary condensation has finished. One must be careful to avoid macroscopic condensation, which is accomplished by removing the substrate from the weighing bottle while it is still in the oven, and only then removing the weighing bottle [41]. The weighing bottles were cleaned in a base bath (KOH (EMD):2-propanol(VWR):H_2O 0.3:3.14:1, by weight), scrubbed with detergent solution, and rinsed in DI water and dried in the oven prior to use.

Fig. 48. Capillary condensation setup. Substance to be condensed (colored orange for clarity) in a 2 mL glass vial is placed inside a secondary 20 mL glass vial, and then inside a large weighing bottle containing the substrate.

F. Instruments

1. Optical Microscopy

a. Model

Optical microscopy images were obtained with a Zeiss Imager.M2m.

2. FTIR

a. Model

Infrared measurements were made with a Bruker Alpha FTIR, using the transmission module.

b. Theory

Infrared microscopy involves analyzing the interaction of the sample with infrared radiation. If the energy of a particular infrared wavelength matches that of the chemical bond, absorption occurs. Chemical bonds have different stretching frequencies and multiple vibration modes (stretching, bending, scissoring, etc.). Plotting absorption peaks versus wavenumber (cm^{-1}) generates an FTIR spectrum.

c. Sample Preparation

Zinc Selenide (ZnSe) disks were used as a substrate, as it is highly transmitting of IR frequencies. In some instances, the sample is already on a substrate (ex. fcc array of silica spheres on a clean silicon wafer), in which case the substrate is used as background (silicon is FTIR-transparent, but only at wavenumbers of 1613 cm^{-1} and greater [49]). The changes in humidity are considered negligeable, and thus ZnSe and silicon wafer spectra are saved as background files to be subtracted instead of being

scanned anew for every FTIR spectrum.

3. Scanning Electron Microscopy

a. Model

Scanning Electron Microscopy (SEM) images were obtained using an ultra high resolution field emission scanning electron microscope (FE-SEM) JEOL JSM-7500F; use of the TAMU Materials Characterization Facility is acknowledged. SEM images in Figure 45, part B and C, and Figure 32, part C were obtained using a Hitachi S-5200 at University of Toronto by Ilya Gourevich.

b. Theory

SEM is based on the interaction of a high-energy beam of electrons with a sample. While many different interactions (x-rays, electrons, cathodoluminescence) are produced by the sample due to contact with the electron beam, the SEM is primarily interested in collecting and mapping secondary electrons (SE) and back-scattered electrons (BSE). Electrons from the incident beam can interact elastically and inelastically with the electric field of atoms in the sample. Inelastic interactions result in transfer of energy from incident electron to the sample, in which case a sample electron is ejected, termed a secondary electron (SE). During elastic interaction, the incident electron changes its trajectory without significant change in its energy. If this electron is deflected back out of the sample, it is termed a backscattered electron (BSE). The fraction of electrons backscattered varies strongly with atomic number, and thus heavier elements appear brighter in the SEM image. JEOL JSM-7500F also has a unique gentle beam (GB) mode, which decelerates the electron beam right before contact with the specimen and helps reduce sample charging without compromising

image resolution common to low acceleration voltages.

c. Sample Preparation

Samples on silicon wafers are imaged directly, while liquid dispersions are deposited on small and clean pieces of silicon wafer and dried before imaging. In most instances, even non-conductive samples (ex. silica particles) can be imaged well using the GB mode. In certain situations (ex. close-packed silica array with many layers), 2 nm of Pd/Pt is deposited using Cressington Sputter Coater 208HR to reduce sample charging. By default, all SEM images in this thesis are SE, unless otherwise specified (ie BSE).

4. Energy-Dispersive X-ray Spectroscopy

a. Model

Energy-Dispersive X-ray (EDX) spectra were obtained using the Oxford EDS system equipped with X-ray mapping and digital imaging, connected to the FE-SEM JEOL JSM-7500F.

b. Theory

A type of X-ray fluorescence spectroscopy, EDX is based on how a high-energy beam of charged particles (in this case, a beam of electrons) interacts with the sample. When the electron beam has energy that is greater than the critical binding energy (energy required to free an electron from a binding orbital of a given element), the incident beam can excite and eject an electron in the inner shell, creating a hole in its place. An electron from an outer shell (higher energy) fills the hole, and in the process an x-ray is emitted with a frequency that corresponds to the energy difference

between the shells. These x-rays are element- and shell-specific, and can thus be used to identify elements and their location within the sample.

c. Sample Preparation

The electron beam acceleration voltage of FE-SEM is at least 1.5 times larger than the x-ray energy (keV) of a given EDX peak. The sample preparation is similar to that of SEM, though no conductive coating is ever deposited on the surface. Sample working distance is optimized for maximum x-ray detection by the EDS detector.

5. Zeta Potential

a. Model

Zeta potential data was obtained using Brookhaven Instruments ZetaPALS Zeta Potential Analyzer. The Smoluchowsky zeta potential model was used to analyze the data.

b. Theory

Zeta potential is the electric potential in the interfacial double layer at the slipping plane, and can be used to infer the charge density of the particle and colloidal particle stability. The zeta potential sign corresponds to the surface charge, with absolute values more than 30-40 mV considered stable dispersions. A zeta potential of zero corresponds to the isoelectronic point. The ZetaPALS system measures electrophoretic mobility via scattered light from a laser source, which can be converted into zeta potential.

c. Sample Preparation

Each sample was allowed to equilibrate while stirring for at least 1 hr, followed by at least 5 minutes of equilibration in the cuvette with the immersed electrode before zeta potential measurement. Each sample measurement is composed of 10 cycles, with 30 cycles/run.

6. Photography

All photographs were taken using a SONY Cyber-shot DSC-W220 (12.1 megapixel).

CHAPTER VI

CURRENT RESEARCH PROJECTS

A. Janus Particles

Janus particles are compartmentalized colloids (one of the three states of matter finely dispersed in another, with at least one dimension in the range from several nm to a few μm) that have 2 different sides of chemistry or polarity. Typically, these particles are larger than molecules, but small enough to sustain Brownian motion [2]. Some possible architectures can be seen in Figure 49 [6]. We are focusing on making both bicompartmental Janus particles and acorn- and snowman-like particles.

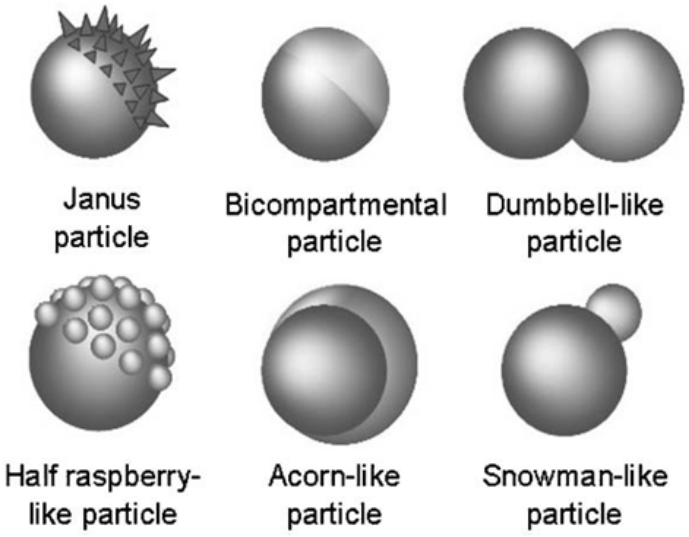

Fig. 49. Possible Janus particle architectures [6].

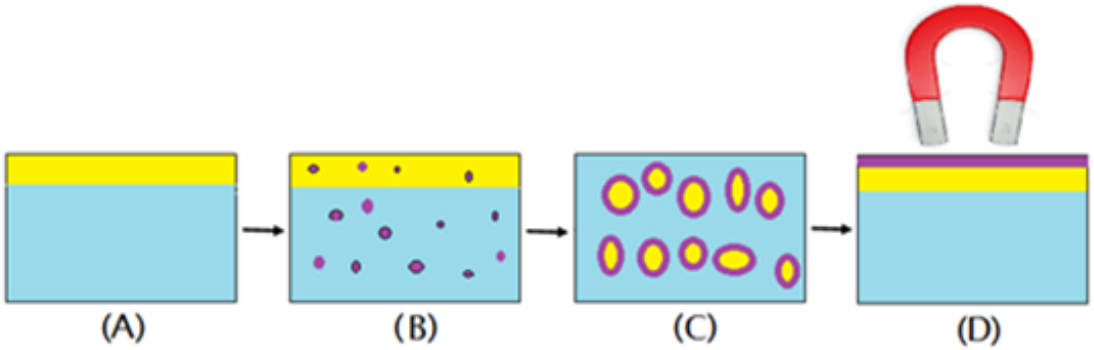

Fig. 50. A - two immiscible liquids not yet emulsified, B - magnetized Janus particles being added to the system, C - stabilized Pickering emulsion being formed by the Janus particles dispersing the yellow liquid in the blue liquid, D - magnetic Janus particles aligned by application of magnetic field destabilizing the emulsion system for easy recovery of the yellow liquid and reuse of the particles.

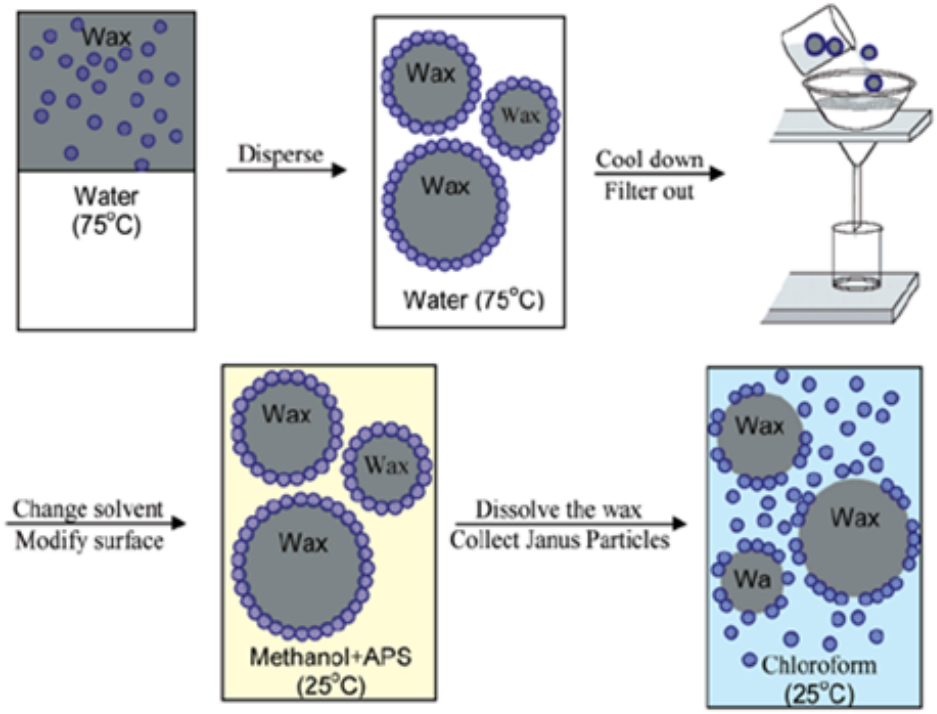

Fig. 51. A schematic of the synthetic route followed in the lab to generate Janus Particle Scavengers [7].

1. Emulsion Stabilization: Oil and Heavy Metal Remediation

Janus particles have many potential applications, and we are specifically interested in emulsion stabilization. It is well-known that small particles can stabilize immiscible liquids forming so-called Pickering emulsions. Unlike surfactants, colloidal particles create more stable emulsions since more energy is required to remove them from the interface [13]. Better yet, Janus particles offer a 3-fold emulsifier potential for water-oil emulsions over homogeneous colloidal particles in theoretical studies [12]. We are interested in making novel magnetite Janus particle scavengers to be used as an emulsifier in place of current surfactants for remediation of contaminated water bodies. Figure 50 shows a schematic of Janus particles used to emulsify and ultimately release, in a controlled manner, hydrocarbons or heavy metals. The Janus particles can form stable emulsions that will entrap oil or heavy metals depending on the ligands attached to the particle. The emulsion can consequently be destabilized by application of a magnetic field which will allow recovery and recycling of the particles and collection and disposal of the toxic waste including oil or heavy metals. Various functionalizations of magnetite Janus particles are tested in the lab for emulsion stability and efficacy of oil, chemicals and heavy metals release, and will be finally used in the field in contaminated estuary, wetland and waterway samples.

Multiple synthetic routes for Janus particle formation exist, and the one currently used in our lab is the masking/unmasking technique, based on work by Hong *et al.* [7] and depicted in Figure 51 [7]. The versatility of the method is its higher yield compared to other available methods and the ability to functionalize one or both sphere sides using wet chemistry. A brief procedure of Janus particle formation is explained below and shown in the schematic in Figure 51.

- Magnetite-coated silica particles, chosen for their low toxicity [57], are synthe-

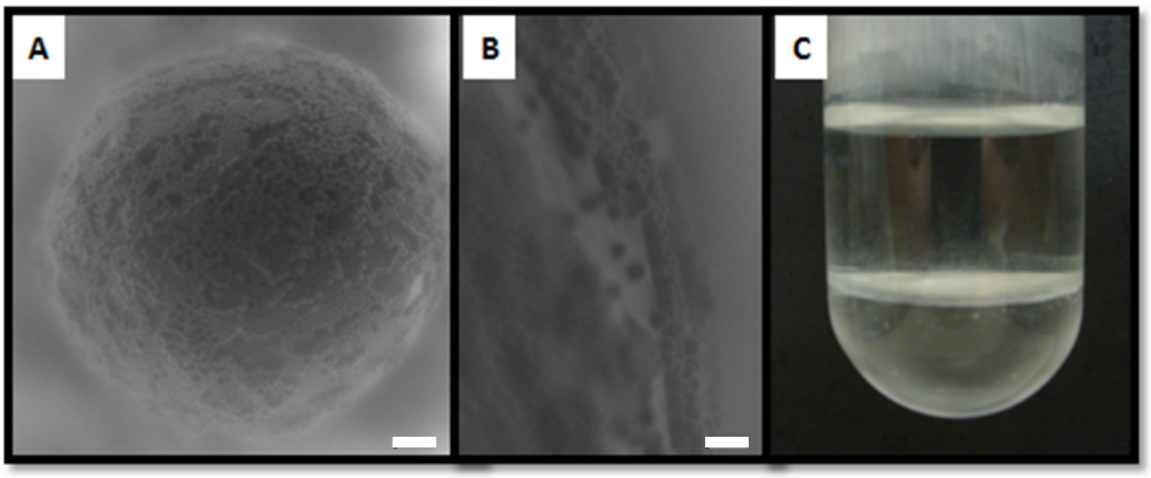

Fig. 52. A - 410 nm silica-in-wax particle, B - particle in A viewed from the side, C - APTES- and TCFS-functionalized 410 nm silica particles, at interface of water and cyclohexane, even after prolonged centrifugation. Scale bar = 1 μm.

sized in the lab and then are suspended in liquid wax at $75°C$. Water is added and an emulsion is formed.

- The emulsion is cooled and then filtered.
- Suitable solvent system is used to functionalize the exposed faces of the silica spheres to desired ligands.
- Wax is then dissolved in chloroform and the functionalized silica particles retrieved.
- The newly exposed surface of the silica can be further functionalized.

We have synthesized silica Janus particles of various sizes (150 nm, 410 nm, 800 nm) functionalized with APTES (3-aminopropyltriethoxysilane) and TCFS (trichloro (1H,1H,2H,2H-perfluorooctyl)silane). Figure 52 shows some exemplary images for 410 nm silica particles. We are currently working on synthesizing Janus silica-coated magnetite particles, and will be testing for emulsification capabilities soon.

2. Polyelectrolyte Complex Particles

The masking/unmasking technique described previously can be extended to making acorn- and snoman-like particles. In particular, if Janus particles of two different sizes are synthesized, one having a positive charge on half of the surface, and the other a negative charge on half of the surface, it is possible to envision the complexing of said particles via electrostatic attraction. We are interested in functionalizing the particles by adsorbing polyelectrolyte on half the particle surface, as shown in Figure 53. Polyelectrolytes currently used for this work are PAH (poly(allylamine hydrochloride)), a polycation and PAA (poly(acrylic acid)), a polyanion, both weak polyelectrolytes. Silica particles, synthesized in the lab via Stöber [45] and Giesche

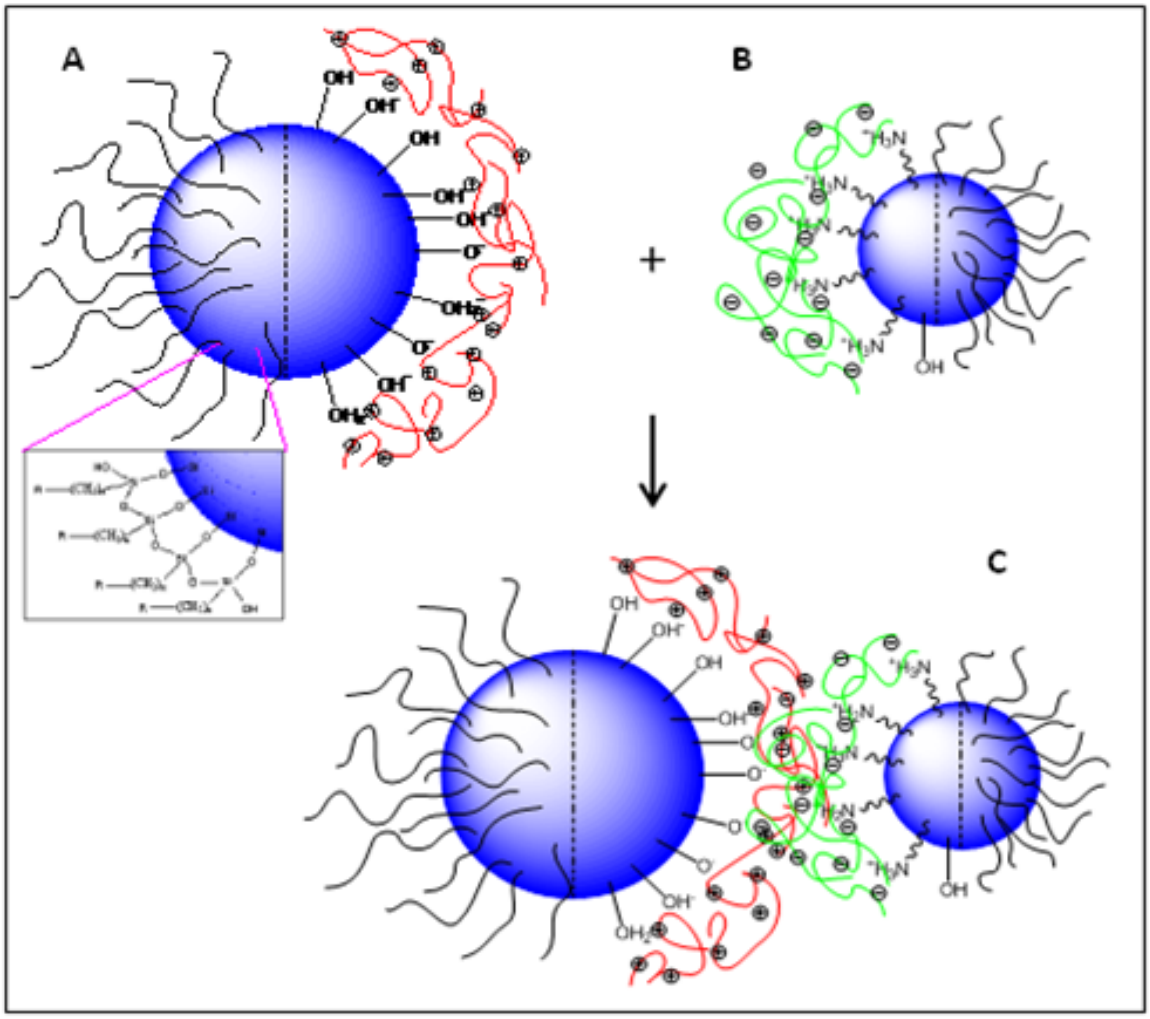

Fig. 53. Janus silica particle functionalized with (A) polyanion and (B) polycation on half the surface, and with octyltrichlorosilane (OTS) on the other half, A inset - OTS attached to silica surface, C - snowman-like Janus particle formed by complexing A and B.

[46, 47] methods, contain pendant hydroxyl groups that can be used for chemical functionalization. Figure 53 A shows a particle functionalized with a polycation on the right hemisphere, and with octyltrichlorosilane (OTS) on the left. Inset of Figure 53 A shows the chemical surface of the OTS-functionalized hemisphere. Figure 53 B shows a particle functionalized with a polyanion on the left hemisphere. In this case, 3-aminopropyltriethoxysilane (APTES) is first reacted with this hemisphere to render the surface positively charged via pendant amine groups, after which the polyanion is attached. Figure 53 C shows the mixing of polyanion and polycation Janus particles of different sizes to form a snowman-like particle.

Preliminary results indicate successful functionalization of silica particles with polyelectrolytes, based on typical zeta potential measurements seen in Table IV. pH values for zeta potential measurements were chosen based on pK_a values of PAH [58] and PAA, which are 8.5 and 6, respectively. At these pH values (9 and 5 for PAH and PAA, respectively), the polyelectrolytes have medium charge density, which will allow adsorption to the silica surface, as well as leave some unadsorbed charged groups on the polyelectrolyte surface for particle complexation. The zeta potential values indicate that the Janus particles (line 3 and 5 of Table III) have zeta potential values intermediate to bare silica particle (line 1) and fully covered PAH (line 2) and APTES + PAA (line 4) particles, which confirms successful partial coverage and Janus nature of the particles. The next step is to functionalize the other hemisphere with OTS, increase particle yield and test formation of snowman-like particles.

Table IV. Zeta potential values for 410 nm and 800 nm silica Janus particles

Sample	pH	Zeta Potential (mV)
1) 400 nm, as synthesized	9	-65.46
2) 400 nm, PAH (fully covered)	9	51.83
3) 400 nm, Janus PAH	9	-18.42
4) 400 nm, APTES + PAA (fully covered)	5	-84.03
5) 400 nm, Janus APTES + PAA	5	-39.79
6) 800 nm, as synthesized	9	-70.09
7) 800 nm, PAH (fully covered)	9	67.57
8) 800 nm, Janus PAH	9	-19.24
9) 800 nm, APTES + PAA (fully covered)	5	-75.30
10) 800 nm, Janus APTES + PAA	5	-44.46

CHAPTER VII

SUMMARY

An extensive literature review of both Janus and patchy particles has been presented in the first two chapters of this thesis. Janus particles, or compartmentalized colloids with 2 different sides of chemistry of polarity, have been introduced in terms of current synthetic methods and applications in Chapter II. Some current research projects involving Janus particles, specifically their novel synthetic routes (Janus dumb-bell particles functionalized and complexed using polyelectrolytes) and employing Janus particles for heavy metal and oil recovery via emulsion stabilization, were briefly discussed in Chapter VI. Patchy particles, or patterned colloidal particles with at least one well-defined patch that can have highly directional and strongly anisotropic interactions with other particles or surfaces, were described in Chapter III. The main synthetic methods for patchy particles (templating, colloidal clusters, particle and nanosphere lithographies, glancing angle deposition and capillary fluid flow) have been discussed, as well as their possible applications.

The body of the thesis, which details a novel synthetic route for patchy particles using capillary condensation, was discussed in Chapter IV and Chapter V. Starting with a thermodynamic background of capillary condensation, the novel patchy particle synthesis was described step-by-step, with synthetic details for all nano- and colloidal particles provided in Chapter V. In essence, colloidal silica particles were ordered into close-packed arrays via evaporative self-assembly and various reagents were capillary condensed into the voids of this assembly. Due to the fcc crystal structure of the colloidal silica array, distinct "patches" of the reagent were produced on the particle surface by capillary condensation. These patches were successfully functionalized with gold nanoparticles, and it was shown that the patch size could be

tuned by the particle diameter inside the fcc array during capillary condensation.

The patchy nature of the resultant particles was confirmed using infrared spectroscopy, scanning electron and optical microscopies, energy dispersive x-ray analysis and zeta potential measurements. SEM images demonstrated gold patches on particles of various sizes, and a general decrease in patch size has been observed with increasing silica particle size. EDX and FTIR spectroscopy confirmed successful capillary condensation of MPES, as well as the absence of any undesired macrocondensation. Zeta potential measurements of APTES-functionalized particles confirmed their patchy nature since the zeta potential of patchy particles, which were partially covered in APTES, was intermediate to zeta potential of particles with full APTES coverage and bare colloidal silica particles. While the functionalization did not have 100% yield, numerous reasons were proposed to explain this, including possible steps and further experiments to mitigate the problem. Finally, surface-enhanced Raman spectroscopy (SERS) was discussed as a possible application for the novel patchy particles made using capillary condensation.

REFERENCES

[1] E. Bianchi R. Blaak and C. N. Likos, "Patchy colloids: State of the art and perspectives," *Physical Chemistry Chemical Physics*, vol. 13, pp. 6397–6410, 2011.

[2] S. Jiang and S. Granick, "Janus balance of amphiphilic colloidal particles," *Journal of Chemical Physics*, vol. 127, pp. 161102–1–161102–4, 2007.

[3] P. G. de Gennes, "Soft matter," *Reviews of Modern Physics*, vol. 64, pp. 645–648, 1992.

[4] A. Walther and A. H. E. Muller, "Janus particles," *Soft Matter*, vol. 4, pp. 663–668, 2008.

[5] K. D. Hartlen A. P. T. Athanasopoulos and V. Kitaev, "Facile preparation of highly monodisperse small spheres (15 to > 200 nm) suitable for colloidal templating and formation of ordered arrays," *Langmuir*, vol. 24, pp. 1714–1720, 2008.

[6] A. Perro S. Reculusa S. Ravaine E. Bourgeat-Lami and E. Duguet, "Design and synthesis of Janus micro- and nanoparticles," *Journal of Materials Chemistry*, vol. 15, pp. 3745–3760, 2005.

[7] L. Hong S. Jiang and S. Granick, "Simple method to produce Janus colloidal particles in large quantity," *Langmuir*, vol. 22, pp. 9495–9499, 2006.

[8] T. Nisisako T. Torii T. Takahashi and Y. Takizawa, "Synthesis of monodisperse bicolored Janus particles with electrical anisotropy using a microfluidic co-flow system," *Advanced Materials*, vol. 18, pp. 1152–1156, 2006.

[9] J. R. Howse R. A. L. Jones A. J. Ryan T. Gough R. Vafabakhsh and R. Golestanian, "Self-motile colloidal particles: From directed propulsion to random walk," *Physical Review Letters*, vol. 99, pp. 048102(1)–048102 (4), 2007.

[10] S. Park J.-H. Lim S.-W. Chung and C. A. Mirkin, "Self-assembly of mesoscopic metal-polymer amphiphiles," *Science*, vol. 303, pp. 348–351, 2004.

[11] Q. Chen S. C. Bae and S. Granick, "Directed self-assembly of a colloidal kagome lattice," *Nature*, vol. 469, pp. 381–384, 2011.

[12] B. P. Binks and P. D. I. Fletcher, "Particles adsorbed at the oil-water interface: A theoretical comparison between spheres of uniform wettability and "Janus" particles," *Langmuir*, vol. 17, pp. 4708–4710, 2001.

[13] B. P. Binks, "Particles as surfactants - Similarities and differences," *Current Opinion in Colloid & Interface Science*, vol. 7, pp. 21–41, 2002.

[14] A. Walther K. Matussek and A. H. E. Muller, "Engineering nanostructured polymer blends with controlled nanoparticle location using Janus particles," *ACS Nano*, vol. 2, pp. 1167–1178, 2008.

[15] Z. Zhang and S. C. Glotzer, "Self-assembly of patchy particles," *Nano Letters*, vol. 4, pp. 1407–1413, 2004.

[16] S. C. Glotzer and M. J. Soloman, "Anisotropy of building blocks and their assembly into complex structures," *Nature Materials*, vol. 6, pp. 557–562, 2007.

[17] A. B. Pawar and I. Kretzchmar, "Fabrication, assembly, and application of patchy particles," *Macromolecular Rapid Communications*, vol. 31, pp. 150–168, 2010.

[18] J.-Q. Cui and I. Kretzschmar, "Surface-anisotropic polystyrene spheres by electroless deposition," *Langmuir*, vol. 22, pp. 8281–8284, 2006.

[19] A. Perro F. Meunier V. Schmitt and S. Ravaine, "Production of large quantities of "Janus" nanoparticles using wax-in-water emulsions," *Colloids and Surfaces A: Physicochemical and Engineering Aspects*, vol. 332, pp. 57–62, 2009.

[20] V. Rastogi A. A. Garcia M. Marquez and O.D. Velev, "Anisotropic particle synthesis inside droplet templates on superhydrophobic surfaces," *Macromolecular Rapid Communications*, vol. 31, pp. 190–195, 2010.

[21] V. N. Manoharan M. T. Elsesser and D. J. Pine, "Dense packing and symmetry in small clusters of microspheres," *Science*, vol. 301, pp. 483–487, 2003.

[22] Y.-S. Cho G.-R. Yi J.-M. Lim S.-H. Kim V. N. Manoharan D. J. Pine and S.-M. Yang, "Self-organization of bidisperse colloids in water droplets," *Journal of the American Chemical Society*, vol. 127, pp. 15968–15975, 2005.

[23] K. E. Sung S. A. Vanapalli D. Mukhija H. A. McKay J. M. Millunchick M. A. Burns and M. J. Solomon, "Programmable fluidic production of microparticles with configurable anisotropy," *Journal of the American Chemical Society*, vol. 130, pp. 1335–1340, 2008.

[24] C. E. Snyder A. M. Yake J. D. Feick and D. Velegol, "Nanoscale functionalization and site-specific assembly of colloids by particle lithography," *Langmuir*, vol. 21, pp. 4813–4815, 2005.

[25] A. M. Yake C. E. Snyder and D. Velegol, "Site-specific functionalization on individual colloids: Size control, stability, and multilayers," *Langmuir*, vol. 23, pp. 9069–9075, 2007.

[26] C. E. Snyder M. Ong and D. Velegol, "In-solution assembly of colloidal water," *Soft Matter*, vol. 5, pp. 1263–1268, 2009.

[27] A. B. Pawar and I. Kretzschmar, "Patchy particles by glancing angle deposition," *Langmuir*, vol. 24, pp. 355–358, 2008.

[28] A. B. Pawar and I. Kretzschmar, "Multifunctional patchy particles by glancing angle deposition," *Langmuir*, vol. 25, pp. 9057–9063, 2009.

[29] G. Zhang D. Wang and H. Mohwald, "Patterning microsphere surfaces by templating colloidal crystals," *Nano Letters*, vol. 5, pp. 143–146, 2005.

[30] G. Zhang D. Wang and H. Mohwald, "Decoration of microspheres with gold nanodots giving colloidal spheres valences," *Angewandte Chemie International Edition*, vol. 44, pp. 7767–7770, 2005.

[31] C. A. Serra and Z. Chang, "Microfluidic-assisted synthesis of polymer particles," *Chemical Engineering & Technology*, vol. 31, pp. 1099–1115, 2008.

[32] K. W. Bong K. T. Bong D. C. Pregibon and P. S. Doyle, "Hydrodynamic focusing lithography," *Angewandte Chemie International Edition*, vol. 49, pp. 87–90, 2010.

[33] K.-H. Roh D. C. Martin and J. Lahann, "Triphasic nanocolloids," *Journal of the American Chemical Society*, vol. 128, pp. 6796–6797, 2006.

[34] K.-H. Roh D. C. Martin and J. Lahann, "Biphasic Janus particles with nanoscale anisotropy," *Nature Materials*, vol. 4, pp. 759–763, 2005.

[35] C. M. Liddell C. J. Summers and A. M. Gokhale, "Stereological estimation of the morphology distribution of ZnS clusters for photonic crystal applications," *Materials Characterization*, vol. 50, pp. 69–79, 2003.

[36] R. Langer and D. A. Tirrell, "Designing materials for biology and medicine," *Nature*, vol. 428, pp. 487–492, 2004.

[37] M. Grätzel, "Photoelectrochemical cells," *Nature*, vol. 414, pp. 338–344, 2001.

[38] J. N. Israelachvili, *Intermolecular and Surface Forces*, Academic Press, Burlington, MA, 3rd edition, 2011.

[39] J. A. Champion Y. K. Katare and S. Mitragotri, "Making polymeric micro- and nanoparticles of complex shapes," *Proceedings of the National Academy of Sciences*, vol. 104, pp. 11901–11904, 2007.

[40] P. Decuzzia and M. Ferraric, "The adhesive strength of non-spherical particles mediated by specific interactions," *Biomaterials*, vol. 27, pp. 5307–5314, 2006.

[41] Z. Gemici P. I. Schwachulla E. H. Williamson M. F. Rubner and R. E. Cohen, "Targeted functionalization of nanoparticle thin films via capillary condensation," *Nano Letters*, vol. 9, pp. 1064–1070, 2009.

[42] P. C. Hiemenz and R. Rajagopalan, *Principles of Colloid and Surface Chemistry*, Marcel Dekker, New York, 3rd edition, 1997.

[43] L. R. Fischer and J. N. Israelachvili, "Direct experimental verification of the Kelvin equation for capillary condensation," *Nature*, vol. 277, pp. 548–549, 1979.

[44] F. Yan and W. A. Goedel, "The preparation of mesoscopic rings in colloidal crystal templates," *Angewandte Chemie International Edition*, vol. 44, pp. 2084–2088, 2005.

[45] W. Stöber A. Fink and E. Bohn, "Controlled growth of monodisperse silica spheres in the micron size range," *Journal of Colloid and Interface Science*, vol. 26, pp. 62–69, 1968.

[46] H. Giesche, "Synthesis of monodispersed silica powders I. Particle properties and reaction kinetics," *Journal of the European Ceramic Society*, vol. 14, pp. 189–204, 1994.

[47] H. Giesche, "Synthesis of monodispersed silica powders II. Controlled growth reaction and continuous production process," *Journal of the European Ceramic Society*, vol. 14, pp. 205–214, 1994.

[48] P. Jiang J. F. Bertone K. S. Hwang and V. L. Colvin, "Single-crystal colloidal multilayers of controlled thickness," *Chemistry of Materials*, vol. 11, pp. 2132–2140, 1999.

[49] J. A. Dean, *Lange's Handbook of Chemistry*, McGraw-Hill, New York, 15th edition, 1999.

[50] W. M. Haynes, *CRC Handbook of Chemistry and Physics (Internet Version 2011)*, CRC Press/Taylor and Francis, Boca Raton, FL, 91st edition, 2011.

[51] X. Liang Y. Xu G. Sun L. Wang Y. Sun and X. Qin, "Preparation, characterization of thiol-functionalized silica and application for sorption of Pb2+ and Cd2+," *Colloids and Surfaces A: Physicochemical and Engineering Aspects*, vol. 349, pp. 61–68, 2009.

[52] E. Finocchio E. Macis R. Raiteri and G. Busca, "Adsorption of trimethoxysilane and of 3-mercaptopropyltrimethoxysilane on silica and on silicon wafers from vapor phase: An IR study," *Langmuir*, vol. 23, pp. 2505–2509, 2007.

[53] A. Beganskiene V. Sirutkaitis M. Kurtinaitiene R. Juškenas and A. Kareiva, "FTIR, TEM and NMR investigations of Stöber silica nanoparticles," *Materials Science (Medžiagotyra)*, vol. 10, pp. 287–290, 2004.

[54] S. Nie and S. R. Emory, "Probing single molecules and single nanoparticles by surface-enhanced Raman scattering," *Science*, vol. 275, pp. 1102–1106, 1997.

[55] R. K. Iler, *The Chemistry of Silica: Solubility, Polymerization, Colloid and Surface Properties, and Biochemistry*, John Wiley & Sons, New York, 1979.

[56] K. C. Grabar R. G. Freeman M. B. Hommer and M. J. Natan, "Preparation and characterization of Au colloid monolayers," *Analytical Chemistry*, vol. 67, pp. 735–743, 1995.

[57] M. M. Lin H.-H. Kim H. Kim M. Muhammed and D. K. Kim, "Iron oxide-based nanomagnets in nanomedicine: Fabrication and applications," *Nano Reviews*, vol. 1, pp. 4883(1)–4883(17), 2010.

[58] K. Itano J. Choi and M. F. Rubner, "Mechanism of the pH-induced discontinuous swelling/deswelling transitions of poly(allylamine hydrochloride)-containing polyelectrolyte multilayer films," *Macromolecules*, vol. 38, pp. 3450–3460, 2010.

VITA

Nina Olegovna Ivanova received her Honours Bachelor of Science degree in chemistry from University of Toronto in May 2009. She started her Master of Science degree in August 2009 at Texas A&M University at the Adaptive Soft & Colloidal Materials research group with Dr. Nicole Zacharia and received her Master of Science degree in December 2011. Nina Olegovna Ivanova may be reached at nina.ivanova@tamu.edu.

Department of Mechanical Engineering, Materials Division
Texas A&M University
200 Engineering Physics
3123 TAMU
College Station, TX 77843

The typist for this thesis was Nina Ivanova.